Modern fabrication techniques for nanostructures and photonic components

Mikhail Erdmanis

top
level
2 μm

slope

12 μm

55°

bottom
level

Aalto University

Modern fabrication techniques for nanostructures and photonic components

Mikhail Erdmanis

A doctoral dissertation completed for the degree of Doctor of Science (Technology) to be defended, with the permission of the Aalto University School of Electrical Engineering, at a public examination held at the lecture hall AS1 of the TUAS building (Otaniementie 17, Espoo, Finland) on the 5th of December 2014 at 12.

Aalto University
School of Electrical Engineering
Department of Micro- and Nanosciences
Micro and Quantum Systems Group

Supervising professor
Prof. Ilkka Tittonen

Preliminary examiners
Prof. Markku Kuittinen, University of Eastern Finland, Finland
Dr. Gualtiero Nunzi Conti, Institute of Applied Physics, Italy

Opponent
Assistant Prof. Kristinn B. Gylfason, Royal Institute of Technology,
Sweden

441   697
Printed matter

Abstract

   This thesis introduces novel micro- and nanofabrication methods and their applications developed in Micronova, the clean room facilities of Aalto University. The work is performed with silicon, which is robust, stable, and easy to process material with good electrical and optical properties. The developed fabrication methods facilitate technologically challenging types of nanostructures and their fabrication on non-planar surfaces.

The presented research consists of two parts. The first part is focused on nanofabrication, mostly via top-down fabrication approach. The second one describes the modification of photonic devices and waveguides by \mbox{atomic-layer-deposited} thin films. The three main types of processing involved in the thesis are: atomic layer deposition, exposure by focused ion beam, and dry etching.

As a result of this study, several fabrication methods were developed. One of them utilizes focused ion beam lithography for nanofabrication on multilevel and strongly corrugated surfaces. This process has a great potential for general 3D integration and for micro- and nanofluidics. The same approach enables the fabrication of suspended nanostructures and gives a platform for accurate measurement of material properties and realization of lab-on-a-chip concepts. Another separately developed process is a grayscale lithography that provides a control over the height of patterned features at nanometer scale. It gives an effective way to fabricate miniature diffractive optics components for extreme ultraviolet and soft X-ray radiation. It also allows for new designs and improved performance of photonic grating couplers. Finally, the work shows how atomic layer deposition can be used to tune the operational parameters of photonic components. In particular, the dispersion properties of photonic nanostrip waveguides were optimized, and microring resonators were tuned towards polarization-independent regime in a broad wavelength range.

In summary, the work extends the applications of nanotechnology for sensing and integrated optics. The shown nanofabrication methods provide fast prototyping due to the minimized number of process steps. Atomic layer deposition of thin films was demonstrated to be very effective for tuning of photonic waveguides and devices. The presented techniques and methods have a showcase character and provide a room for further research focused on other materials and applications.

Tiivistelmä

Tässä väitöskirjassa tarkastellaan Aalto-yliopiston Micronova-puhdastilaympäristössä kehitettyjä uusia mikro- ja nanotekniikan valmistusmenetelmiä ja niiden sovelluksia. Valmistusmateriaaliksi valittiin pii, koska se on kestävä ja stabiili materiaali, jolla on suotuisat sähköiset ja optiset ominaisuudet ja jota on verrattain helppo prosessoida.

Työ koostuu kahdesta osasta. Ensimmäinen osa käsittelee nanovalmistusta, pääosin ns. "top-down"- valmistustekniikoita, joihin kuuluu menetelmiä, joilla materiaalia poistetaan ennalta suunnitellun kuvion mukaisesti. Toisessa osassa tutkitaan fotoniikan komponenttien ominaisuuksien räätälöintiä atomikerroskasvatettujen ohutkalvojen avulla. Tässä tutkimustyössä on kolme keskeistä prosessia: atomikerroskasvatus, fokusoidun ionisuihkun avulla suoritettu kuviointi ja kuivaetsaus.

Tutkimuksen tuloksena on kehitetty useita piimateriaalin muokkaamiseen tarkoitettuja valmistusmenetelmiä. Merkittävä osa tuloksista saatiin hyödyntämällä fokusoidun ionisuihkun (FIB) avulla suoritettua litografiaa, jolloin oli mahdollista saada aikaan nanorakenteita myös epätasaisille ja kalteville pinnoille. Tätä prosessia voi hyödyntää sekä 3D-integraatiossa että mikro- ja nanofluidistiikassa. Samoja periaatteita voidaan soveltaa myös vapautettujen nanorakenteiden valmistamiseen. Tämäntyyppisiä rakenteita käytetään mm. materiaalien ominaisuuksien tutkimuksissa ja "lab-on-a-chip"- sovelluksissa. Tutkimuksessa on myös kehitetty fokusoidun ionisuihkun käyttöön perustuva ns. "harmaasävy"- litografia, jolla kyetään aikaansaamaan erilaisia nanorakenteiden korkeusprofiileja. Tätä menetelmää voi käyttää pienten integroitujen diffraktiivisen optiikan komponenttien valmistukseen, jotka toimivat ultraviolettiaallonpituuksilla. Työssä kehitetty litografia mahdollistaa uuden tavan tehdä piipohjaisia fotoniikan hilakytkimiä. Lisäksi tässä väitöskirjassa esitellään tapoja käyttää atomikerroskasvatusta fotoniikassa aaltojohteiden ja mikroresonaattorien virittämiseen esimerkiksi siten, että niiden toiminta on polarisaatiosta riippumaton.

Tässä työssä saavutetut tulokset laajentavat nanoteknologian mahdollisuuksia sekä nanorakenteiden valmistamisessa että optiikan sovelluksissa. Kehitetyissä valmistusmenetelmissä prosessivaiheiden määrä on minimoitu, joten ne sopivat erityisesti prototyyppien valmistamiseen. Työssä esitetään myös suuntaviivoja miten näitä kehitettyjä perustekniikoita voisi jatkossa edelleen tehostaa.

Preface

The research presented in this dissertation has been carried out in the Micro and Quantum Systems group (MQS) of the Department of Micro- and Nanosciences, School of Electrical Engineering at Aalto University. The experimental work has been accomplished in Micronova, the clean room facilities for micro- and nanotechnology research.

I want to express my deepest gratitude to my Professor Ilkka Tittonen who has played a key role in my research and endorsed me for ambitious and far reaching projects. You also showed me the benefits of networking and simultaneous focusing on different areas of physics.

I want to warmly thank the members of MQS group for creating a pleasant working atmosphere and being very supportive. The list starts from Nikolai Chekurov – you were always my ultimate reference is terms of dedication and quality of everything that you do. Your tutoring and fearless solving of any problems were fantastic. I also thank Ville Pale for always being so helpful and positive, Mikko Ruoho for honest and thoughtful critics and comments, Päivi Sievilä for charming smile and great support. I am particularly thankful to Osmo Vänskä – you are an amazing person and you will definitely become a professor one day! And of course, I acknowledge all other present and former members of MQS: Thomas Lindvall, Ossi Kimmelma, Tuomas Rossi, Zhengjun Liu, Julius Nieminen, Jorma Selin, Juha Heinonen...

I would like to acknowledge Fiber Optics group for a vivid and productive start of my PhD during the time period August 2009 – July 2011. I want thank Dr. Igor Shavrin, Dr. Steffen Novotny, and Docent Hanne Ludvigsen for their highly professional supervising and support.

I am exceptionally grateful to Dr. Victor Ovchinnikov. You have a very special place in my PhD journey. Your superb knowledge of physics, deep analytical skills, and expertise of handling the most demanding pieces of

equipment allowed us to find the answers and achieve the results we have been looking for.

I want to acknowledge the Photonics group lead by Professor Seppo Honkanen and Docent Ari Tervonen. Your group had a magnificent team spirit and working with you was an outstanding experience. I am grateful to Antti Säynätjoki, Lasse Karvonen, Joan Jesus Montiel i Ponsoda, Ya Chen, and Tapani Alasaarela.

I want to give credits to people who did their best to provide the smooth operation of the Micronova clean room: Veli-Matti Airaksinen, Paula Heikkilä, Risto Salo, Paula Kettula, Antti Peltonen...

I want to warmly thank all people with whom I had a pleasure to meet or collaborate with at different stages: Outi Toikkanen, Doan Thi Minh Nguyet, Aleksandr Kravchenko, Andrey Shchepetov, Ali Shah, Esa Tuovinen, Gianmario Scotti, Alexander Pyymäki Perros, Matthias Meschke, Olli Svensk, Andriy Shevchenko, Patrick Grahn, Sami Suihkonen, Sami Kujala, Marco Mattila, Päivi Mattila, Kimmo Kokkonen, Markku Kapulainen, Professor Kari Halonen, Kirsi Toivola, Professor Robin Ras, Professor Sami Franssila, and Professor Harri Lipsanen.

I am obliged to pre-examiners, Professor Markku Kuittinen and Dr. Gualtiero Nunzi Conti, for their very thorough scrutiny of this thesis.

Finally, I would like to express my deepest gratitude to my parents and my family for their unconditional and everlasting love, support, and encouragement.

Espoo, October 26, 2014,

Mikhail Erdmanis

Contents

List of Publications

This thesis consists of an overview and of the following publications which are referred to in the text by their Roman numerals.

I O. Toikkanen, N. Doan, M. Erdmanis, K. Kontturi, H. Lipsanen, and B. Parviz. Building molecular surface gradients with electron beam lithography. *Journal of Micromechanics and Microengineering*, vol. 21, pp. 054025–1–5, 2011.

II M. Erdmanis, P. Sievilä, A. Shah, N. Chekurov, V. Ovchinnikov, and I. Tittonen. Focused ion beam lithography for fabrication of suspended nanostructures on highly corrugated surfaces. *Nanotechnology*, vol. 25, pp. 335302–1–7, 2014.

III M. Erdmanis and I. Tittonen. Focused ion beam high resolution grayscale lithography for silicon-based nanostructures. *Applied Physics Letters*, vol. 104, pp. 073118–1–5, 2014.

IV M. Erdmanis, L. Karvonen, A. Säynätjoki, X. Tu, T. Y. Liow, Q. G. Lo, O. Vänskä, S. Honkanen, and I. Tittonen. Towards broad-bandwidth polarization-independent nanostrip waveguide ring resonators. *Optics Express*, vol. 21, pp. 9974–9981, 2013.

V M. Erdmanis, L. Karvonen, M. R. Saleem, M. Ruoho, V. Pale, A. Tervonen, S. Honkanen, and I. Tittonen. ALD-assisted multiorder dispersion engineering of nanophotonic strip waveguides. *Journal of Lightwave Technology*, vol. 30, pp. 2488–2493, 2012.

Author's Contribution

Publication I: "Building molecular surface gradients with electron beam lithography"

The author did the e-beam lithography, SEM imaging, and participated in the planning of experiments and the preparation of the manuscript.

Publication II: "Focused ion beam lithography for fabrication of suspended nanostructures on highly corrugated surfaces"

The author had a major role in this publication. He was in charge of the process development and optimization, design of the structures, nanofabrication, and the preparation of the manuscript.

Publication III: "Focused ion beam high resolution grayscale lithography for silicon-based nanostructures"

The author had a major role in this publication. He was in charge of the process development and optimization, design of the structures, nanofabrication, and the preparation of the manuscript.

Publication IV: "Towards broad-bandwidth polarization-independent nanostrip waveguide ring resonators"

The author had a major role in this publication. He was in charge of atomic layer deposition, sample characterization, data postprocessing, numerical analysis, and the preparation of the manuscript.

Publication V: "ALD-assisted multiorder dispersion engineering of nanophotonic strip waveguides"

The author had a major role in this publication. He was in charge of the theoretical research, numerical simulations, and the preparation of the manuscript.

List of abbreviations

AFM	Atomic force microscopy
ALD	Atomic layer deposition
Al_2O_3	Aluminum oxide
$Al(CH_3)_3$	Trimethylaluminum
Au	Gold
CCP	Capacitively coupled plasma
CMOS	Complementary metal-oxide-semiconductor
DC	Direct current
DOF	Depth of focus
e-beam	Electron beam
EBL	Electron beam lithography
F	Fluorine
FEM	Finite element method
FIB	Focused ion beam
FIBL	Focused ion beam lithography
FSR	Free spectral range
FWHM	Full width at half maximum
Ga	Gallium
GVD	Group velocity dispersion
H_2O	Water

ICP	Inductively coupled plasma
ICP-RIE	Reactive ion etching with inductively coupled plasma
IR	Infrared
LMIS	Liquid metal ion source
MDW	Minimum-dispersion wavelength
RF	Radio frequency
RIE	Reactive ion etching
SAM	Self-assembled monolayer
SEM	Scanning electron microscopy
Si	Silicon
Si_3N_4	Silicon nitride
SiO_2	Silicon dioxide
SOI	Silicon-on-insulator
$TiCl_4$	Titanium tetrachloride
TiO_2	Titanium dioxide
UV	Ultraviolet
ZDW	Zero-dispersion wavelength

List of symbols

a	Amplitude of electric field [V/m]
c_{o}	The speed of light in vacuum [m/s]
h	Height [m]
I	Intensity [W/m^2]
k_{o}	Wavenumber in vacuum [rad/m]
l	Length [m]
n	Refractive index
n_{eff}	Effective refractive index
n_{g}	Group index
n_2	Nonlinear refractive index [m^2/W]
P	Power [W]
Q	Quality factor
r	Radius [m]
t	Thickness [m]
t'	Amplitude transmission coefficient
w	Width [m]

α'	Resonator internal loss per round trip
β	Propagation constant [1/m]
β_2	Group velocity dispersion parameter [ps^2/m]
λ	Wavelength in material [m]
λ_{o}	Wavelength in vacuum [m]
λ_{res}	Resonance wavelength [m]
ν	Frequency [1/s]
ϕ	Phase [rad]
$\Delta\phi$	Phase mismatch [rad]
$\Delta\phi_L$	Linear part of phase shift [rad]
$\Delta\phi_{NL}$	Nonlinear part of phase shift [rad]
ω	Angular frequency [rad/s]

1. Introduction

Nanofabrication is a set of methods for fabrication of structures where at least one lateral dimension is smaller than 100 nm. It reflects in the quality of our life, playing a crucial role in progress of nanotechnology and making affordable the devices that were unavailable 15-20 years ago. Nanostructuring not only decreases the size of final devices, but also brings along new material properties in comparison to larger microscale structures. Consequently, there is a strong interest to combine effects emerging at nanoscale and microscale to gain new functionalities in surface science [1], semiconductor industry [2], and biomedical applications [3].

Nanofabrication similarly serves for more effective use of various optical phenomena. For example, deposition of nm-thick films can be utilized for high-performance optical coatings [4]. Fabrication of nanoscale features provides new opportunities for precise manipulation of light via resonant periodic structures [5]. In everyday life, such processes and methods already benefit multiple devices, including glasses, cameras, and display systems. Nanofabrication can also boost the efficiency of data transmission in photonics and telecommunication systems.

Many nanofabrication methods have their origins in semiconductor microfabrication. These techniques employ a stable and repeatable top-down fabrication approach, which represents a sequence of fabrication steps that shape the material into a required form. In this case, standard fabrication steps are: formation of mask (deposition), patterning of structure layout (lithography), and etching (or milling) that forms final structure. An alternative way of nanofabrication is known as bottom-up approach, where molecules acquire pre-designed arrangement on a surface and form the desired structure. Very often it utilizes various mechanisms of molecular self-assembly [6, 7, 8]. Bottom-up approach generally has poorer repeatability and higher chances of defect formation.

From multiple materials suitable for micro- and nanofabrication, silicon has become number one in semiconductor industry. The reasons are that silicon is stable, easy to process, and it has good mechanical, electrical, and optical properties. In nanoscience, fabrication from silicon allows for realization of technologically challenging nanostructures and their further implementation into the existing semiconductor platform. At the same time, silicon has a very high refractive index, which ensures strong confinement of light in silicon waveguides and enables the dimensions essentially more compact than those of optical fibers. Consequently, silicon is an important material for micro- and nanofluidics [9, 10], sensing [11], photonics [12], plasmonics and photovoltaic devices [13].

This thesis represents a collection of scientific studies devoted to nanofabrication processes and their potential applications. Publication I presents a simple approach for the formation of nanoparticle gradients through the electron beam exposure of self-assembled monolayers (SAM). Publication II shows a method that enables fabrication of suspended nanonetworks and their patterning on multilevel surfaces. Publication III demonstrates a grayscale lithography that provides custom pre-designed surface profiles with nanoscale resolution. Publication IV illustrates how the application of atomic layer deposition (ALD) technique can be used to control the operation of photonic microring resonators. Finally, Publication V reveals that ALD films can be used to engineer the dispersion properties of photonic nanostrip waveguides.

The main objectives of this thesis were the development of novel nanofabrication routines and introduction of new practices of use for existing techniques. Throughout this work, there is a constant focus on possible applications of investigated methods (e.g. effective tuning of photonic devices or realization of multilevel fabrication). Another goal was optimization, the proposed nanofabrication methods have minimized number of process steps and provide fast prototyping. The same applies to the demonstrated tuning of photonic devices by ALD, where the proposed method can be utilized to process many chips simultaneously.

The thesis is organized as follows. Chapter 2 introduces methods and equipment involved in silicon nanofabrication. It describes different types of fabrication tools and covers the key properties of employed process steps. Chapter 3 presents silicon photonics and gives a theoretical background for certain optical phenomena. It describes properties of light, and principles of operation of photonic waveguides and commonly used photonic devices.

It also discusses the challenges in silicon photonics that are addressed in this thesis. Chapter 4 summarizes the achievements of this work in terms of developed fabrication processes and shown applications. Chapter 5 gives more examples of use of the proposed methods and processes and describes their role in comparison to other approaches.

2. Silicon nanofabrication

2.1 Silicon

Silicon is an Earth-abundant semiconductor material with excellent mechanical, electrical, and optical properties. It can tolerate high temperatures and is compatible with various types of fabrication processes. Since the late 1950s, it has been the main material in semiconductor device industry due to high repeatability of fabrication and stable long-term operation of silicon devices. Nowadays, silicon plays an important role in microelectronics, optoelectronics, photonics, micromechanics, and microfluidics. The commonly known silicon applications from everyday life are associated with CMOS technology, where it is used in microprocessors, memory chips, and various types of sensors.

Silicon (Si) is a crystalline material with the atomic number 14 and a cubic diamond lattice structure (Fig. 2.1). One unit cell has a lattice constant of 5.431 Å, it contains 8 Si atoms, and has a filling ratio of 34 % (a fraction of volume filled by Si atoms). Such a structure results in different mechanical and etching properties along different crystallographic planes.

Single-crystalline silicon is usually obtained via Czochralski growth [14] (at 1420°C in vacuum) where the crystal structure and orientation of
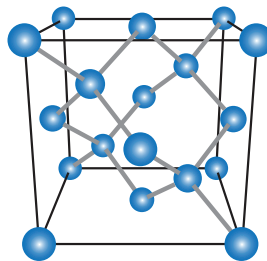
Figure 2.1. Diamond cubic crystal structure of silicon lattice (schematic drawing).

formed silicon ingot is defined by the crystal structure of the seed. Electrical properties of the material are controlled by doping and growth parameters. Formed silicon boule is cut into wafers that are then supplied to industry. The wafers typically have a diameter of 100 to 300 mm and are 300 to 800 μm thick. Production of monocrystalline silicon is expensive and for some applications (such as e.g. solar cells) polycrystalline or amorphous silicon can be used as a low cost alternative. Nevertheless, monocrystalline electronic grade silicon is the ultimate material for nanofabrication due to its highest purity. When it is used, the quality of manufactured silicon structures mostly depends on the technologies and methods employed in fabrication. This thesis addresses the development and optimization of fabrication processes for silicon nanostructures with additional functionalities.

2.2 High resolution lithography

2.2.1 Electron beam and focused ion beam

Electron beam (e-beam) and focused ion beam (FIB) were used as lithography tools for the experimental work presented in this thesis. Both instruments provide nanoscale resolution and have similar basic architectures (shown in Fig. 2.2). Each of the machines includes a source, a focusing system, and a detector. However, there are internal differences in these blocks.
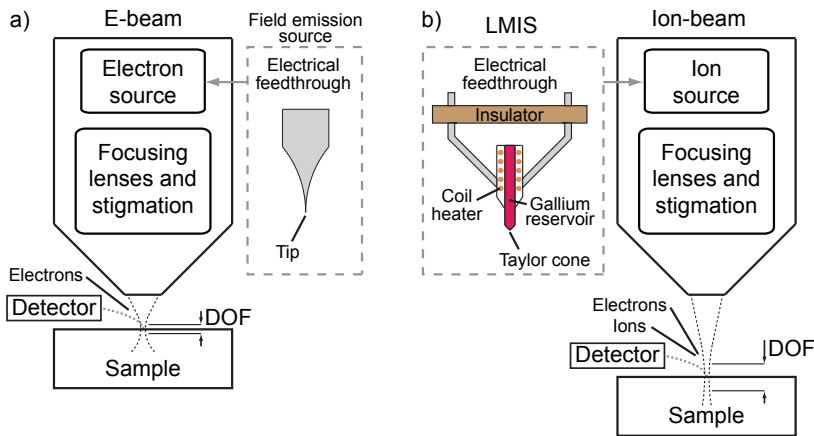
Figure 2.2. Schematic drawing of (a) e-beam and (b) FIB systems. Inlets show commonly used electron and ion sources.

Electron sources employ either field emission or field-assisted thermionic emission from a sharp tip (inlet in Fig. 2.2(a)) in ultra-high vacuum, which is usually better than 10^{-10} mBar. In this case, a very high electric field (reaching 10^8 V/m) created near the tip apex makes electrons tunnel out from a tip. Such electron sources are very popular due to their long lifetime and the small spot size of generated beam.

Most modern ion sources are based on a concept of liquid metal ion source (LMIS), which was invented in 1970s [15]. They provide stable, bright, and highly focused ion beams. Such ion sources do not require ultra-high vacuum (the pressure can be a few orders of magnitude higher than for electron sources). Gallium (Ga) is a commonly used LMIS material due to its low melting temperature (29.77°C), low volatility, and low vapor pressure [16]. A general structure of LMIS is shown in the inlet of Fig. 2.2(b). A reservoir with liquid gallium provides a thin film that covers the needle tip, where a strong electric field creates a Taylor cone and evaporates ions from the tip apex.

Focusing systems of e-beam and FIB have some differences in their operation principles. E-beam typically employs magnetic lenses, whereas in FIB focusing is provided by electrostatic lenses. The reason is that ions are much heavier than electrons and Lorentz force acting on ions is not enough to focus them effectively. In both systems imaging signal is obtained through the detection of generated electrons, however, FIB generally provides better material contrast.

In terms of achievable resolution, both systems can provide a fine beam with a diameter of well below 10 nm. However, with the same current and acceleration voltage, the size of e-beam is smaller. This difference originates from more advanced e-beam focusing systems, and high energy dispersion of focused ions that limits the minimum achievable beam size.

Nevertheless, there is one characteristic where FIB essentially outperforms e-beam, which is called depth of focus (DOF). Depth of focus indicates spatial extent where an imaging object stays in focus (qualitatively illustrated for both systems in Fig. 2.2). Heavy ions diverge more slowly than electrons, and the difference in DOF can exceed one order of magnitude, being 5-10 μm for e-beam and at least 100 μm for FIB [17]. This property gives a significant advantage when patterning is to be performed on irregular or multilevel surfaces.

2.2.2 Interaction of electrons and ions with matter

Figure 2.3 illustrates the main processes that result from interaction of focused electron or ion beam with solid matter [18, 19]. Incident e-beam generates both, electromagnetic (cathodoluminescence, X-rays) and electron signals due to various types of elastic and inelastic collisions. Energy delivered to the sample by electrons allows for modification of surface sensitive layer such as resist, which is used in e-beam lithography.

When an ion beam is irradiated onto a sample, ions can be either reflected (backsputtered) or they can participate in a collision cascade followed by emission of lower energy ions and electrons. The fundamental difference from the e-beam interaction is that since ion beam sputters sample material, it also causes lattice defects, amorphization of crystalline structure, and implantation of ions [19]. Lattice modification and ion implantation are the processes that play an important role in FIB lithography.
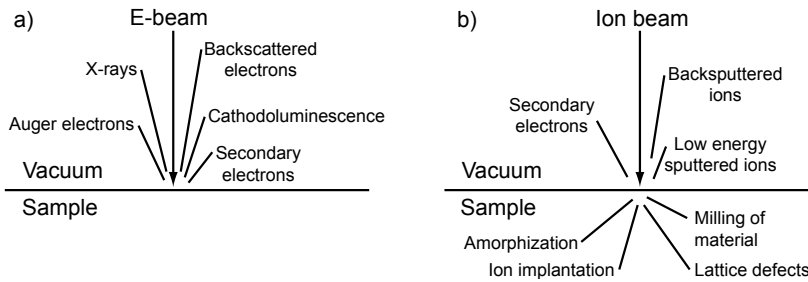
Figure 2.3. Processes induced by irradiation of sample by (a) electron and (b) ion beam.

Penetration depth of electrons and ions characterizes how deep they can propagate into a solid matter. This range is typically defined by the applied acceleration voltage and a sample material. The penetration depth is remarkably different for electrons and ions due to the huge difference in size and mass of the particles. Penetration depth is one of the main parameters that is to be taken into account in e-beam and FIB lithographies. For example, with the acceleration voltage of 30 kV, electrons can penetrate into a material for a few micrometers, while ions will only propagate for 30–40 nm [20]. With larger penetration depths, electrons tend to produce a "halo" around the exposed areas. Such "halos", especially when they overlap with each other, cause an unintentional exposure of resist, known as proximity effect [21]. This effect is stronger for low energy electron beams and it remarkably decreases with higher energy beams. The proximity effects are essentially smaller for focused ion beams in comparison to electron beams of similar energies.

2.2.3 Resist types and properties

Generally, there are two types of resists used in lithography, known as positive and negative tone resists. Solubility or etching speed of positive resists increases upon exposure, while exposed negative resists in contrast become less vulnerable to etching. Figure 2.4 shows how the two types of similarly exposed resists exhibit opposite profiles after resist development, which consequently results in different structures formed by etching.
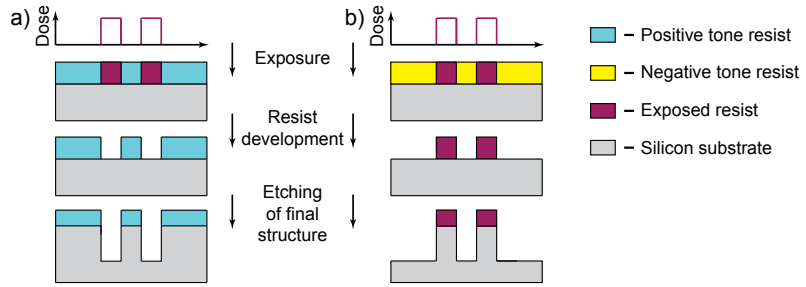
Figure 2.4. Lithography process flow for (a) positive and (b) negative tone resists.

When sample exposure is performed by e-beam, the process is abbreviated as electron beam lithography (EBL). It generally employs polymer-based resists, from which PMMA and Zep-520 are commonly used positive resists, whereas HSQ and SU-8 are standard negative resists. Exposure of positive resist cuts long molecular chains into shorter ones that become soluble in the developer. In the case of negative resist, short-chain molecules are cross-linked upon exposure and become insoluble.

When FIB is used for exposure (referred as focused ion beam lithography, or FIBL), it generates secondary electrons and therefore it can operate with many resists suitable for e-beam lithography [22]. The resolution of FIBL is generally worse than of EBL, however, it has much smaller proximity effects [21] due to the absence of electron backscattering. In addition to polymer-based resists, implantation of ions and modification of surface layer give an opportunity to utilize FIB with a number of inorganic resists. Such positive and negative tone ion-sensitive resists that can be developed by either wet or dry etching have been actively studied for more than 25 years [23, 24, 25, 26]. In inorganic resists, etch-retarding behavior of areas exposed by FIB originate from several mechanisms. One is a physical change of lattice constant and the corresponding strain effects caused by bombarding ions, which slow down wet and dry etching rates [27, 28]. Another is a change of surface chemical reaction in dry

etching, e.g., when areas irradiated by gallium ions promote the formation of nonvolatile masking compound [29, 30] or thin gallium oxide layer [19, 28]. The described masking mechanisms also allow for FIB patterning and subsequent structure formation on bare sample without any photoresist (demonstrated for silicon in [31]).

The two key parameters defining resist properties are its sensitivity and contrast. The parameters are qualitatively illustrated by the development curves in Figs. 2.5(a,b), which indicate resist thickness remaining after resist development (etching) as a function of exposure dose. The curves are given for negative tone resist (corresponds to the process flow shown in Fig. 2.4(b)) since this type of resist was utilized for the nanofabrication schemes discussed in this thesis.
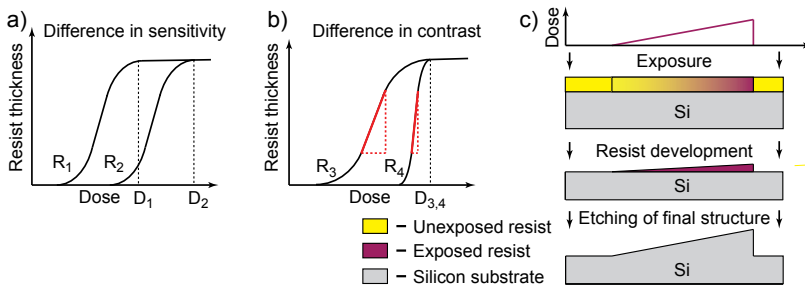
Figure 2.5. Development curves illustrating (a) sensitivity and (b) contrast of resist. (c) Process flow of grayscale lithography with negative tone resist.

Sensitivity of negative tone resist is defined by a dose that is needed to protect resist from removal by etching. In Fig. 2.5(a), resist R1 has a higher sensitivity than R2. Resist contrast is related to a slope of the development curve, as shown in Fig. 2.5(b), where resist R3 has a lower contrast that R4.

In common types of lithographies, sample is exposed by a pattern with a fixed dose (as in Fig. 2.4). Resists with high sensitivity and contrast are generally beneficial due to minimized exposure time and sharp patterned features. In the case of negative tone resists, dose of exposure is selected such a way that a sufficiently thick resist layer remains on a sample after the etching stage (represented by D1 and D2 values in Fig. 2.5(a)).

Grayscale lithography [32] utilizes a different exposure strategy. This type of lithography enables control over height of fabricated structure through local adjustment of resist thickness. In grayscale lithography, resist should be of low contrast in order to provide a wide range of applicable exposure doses. At the same time, accurate control of height profile requires the presence of sufficient linear slope in development curve.

Figure 2.5(c) illustrates the process flow for idealized grayscale lithography, where a spatial linear increase in dose is transferred into a linear profile of resist, and finally into a linear slope of fabricated structure. In reality, achievable results are limited by nonlinear slope of resist development curve and parameters of etching that is used for structure formation.

Until now, grayscale lithography has been widely used with optical [33, 34] and electron [35] beam exposure. In this thesis, I show the realization of a grayscale lithography that is based on the exposure by FIB [Publication III].

2.3 Formation of structure via dry etching

2.3.1 RIE and ICP-RIE

Reactive ion etching (RIE) refers to a dry etching through interaction with weakly ionized reactive gases produced by striking a glow discharge [36]. Such etching contains two components - chemical (due to chemical reactions) and physical (due to ion bombardment). A distinctive property of RIE is the directionality of etching, which occurs because ion bombardment activates chemical reactions predominantly on horizontal surfaces and leaves vertical surfaces almost unaffected. When gas radicals react with the sample material, they form species of high volatility that desorb from a sample surface. In the case of silicon etching with fluorine-based gas mixtures considered in this thesis, the species formed on silicon surface have a SiF_x composition.

Let us consider two different types of RIE reactors that have been used for nanofabrication discussed in this thesis. The first one is simply abbreviated as RIE, it has a parallel plate configuration shown in Fig. 2.6(a) and employs capacitively coupled plasma (CCP). Upper electrode is grounded and gas enters the chamber through it. Lower electrode, which is used for sample mounting, is supplied with a 13.56 MHz RF bias. Reactive gases get ionized due to collisions of accelerated electrons with neutral species. Lower electrode is electrically isolated from the rest of the chamber and consequently it becomes negatively charged due to the differences in mass and velocity between electrons and ions. This effect is known as self-bias, which results in the formation of DC field that accelerates ions towards the substrate. Second type of reactor performs reactive ion etching
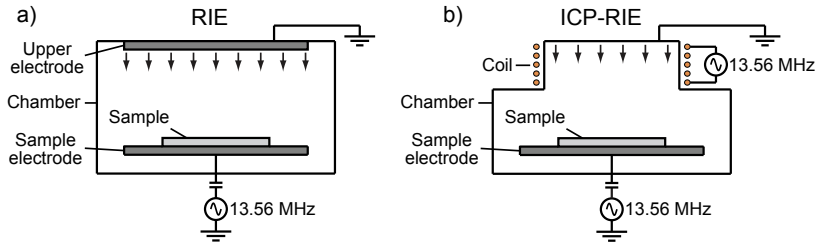
Figure 2.6. (a) RIE reactor in parallel plate configuration and (b) ICP-RIE reactor with magnetic coil. Input flow of reactive gases is indicated by arrows.

with inductively coupled plasma (Fig. 2.6(b)) and is usually abbreviated as ICP-RIE. The main distinctive feature of ICP-RIE is that plasma is also generated remotely by a magnetic coil that is installed on top of the chamber. This allows for very effective generation of plasma and therefore the concentration of plasma in ICP-RIE is significantly higher than in RIE. An important consequence of high plasma concentration is an opportunity to operate ICP-RIE in soft etching regime with very low RF power and DC bias.

2.3.2 Etch selectivity and etch profiles

Fabrication of structures by dry etching requires achievement of particular etching conditions. Optimization of etching can be done through various characteristics. In this dissertation, we will mainly focus on etch selectivity and shape of etch profiles. Selectivity is defined as a ratio between etching speeds of two materials (typically, of mask and masked material). Due to the finite thickness of resist, selectivity defines maximum height of formed structures. Therefore, it has a prime importance in cases when either resist thickness or depth of exposure are strongly limited.

Profiles of structures formed by dry etching determine their usability and possible applications. In general, etching can be classified as isotropic or anisotropic. Etching is said to be isotropic when etching rate is equal in all directions and anisotropic when etching occurs primarily in one direction. Figures 2.7 gives examples of typical etch profiles obtained by dry etching.

Figure 2.7. Examples of structure profiles obtained by dry etching with: (a) low anisotropy, (b) high anisotropy, (c) positive or (d) negative sidewall angles.

Structure shown in Fig. 2.7(a) is obtained when process parameters are shifted towards isotropic etching. Figure 2.7(b) illustrates a case of ideal anisotropic 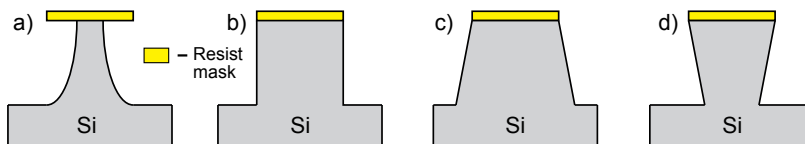etching with sidewall angles of formed structure being equal to 90 degrees. When sidewalls are flat, but they do not form a right angle with a substrate, structure is described as either having positive (Fig. 2.7(c)) or negative (Fig. 2.7(d)) sidewall angles.

Geometry of obtained structures strongly depends on etching parameters. For RIE, these parameters are: RF power, chamber pressure, temperature, and flow of reactive gases. ICP-RIE has the additional control features, such as adjustable ICP power and, for some systems, the possibility to operate at cryogenic temperatures. RIE generally provides better repeatability and lower etching speed, while ICP-RIE has higher anisotropy and selectivity that give more flexibility in terms of final structure profile.

Release is a fabrication step that provides controllable formation of suspended structures. Dry etching is one of commonly used techniques to perform a release [37]. In this case, suspended structures are typically formed at places where mask is intentionally made narrower, while other areas act as supporting blocks. Figure 2.8(a) illustrates an example of such a release, where suspended structure is represented by the bridge on top of two supporting posts. Very often, release is achieved by shifting RIE parameters towards lower anisotropy, which removes underlaying material. If the same mask is etched strictly anisotropically, it will result in a solid structure with 90 degree sidewall angle (Fig. 2.8(b)). Apart from etching with low anisotropy, there are other ways to achieve a release. One of them is to employ high concentration of plasma in ICP-RIE, which intensifies mask undercut. Applications of the described release methods are explored in this thesis.
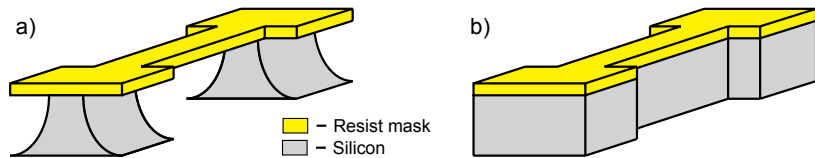

Figure 2.8. (a) Released structure obtained by dry etching with low anisotropy and (b) solid structure formed by anisotropic etching.

2.4 Atomic layer deposition of thin films

2.4.1 Method overview

Atomic layer deposition (ALD) is a chemical vapor deposition technique that employs sequential self-terminating gas-solid chemical reactions [38]. The method can be applied to deposit both conductive and non-conductive materials [39].

Each cycle of ALD process typically consists of four different steps, as illustrated in Fig. 2.9(a). The operation principle is that reactive gases are let (pulsed) into a chamber sequentially in order to avoid their reaction with each other. During the pulse cycle, precursor gas reacts with surface groups in a saturative way. Consequently, a number of precursor molecules absorbed on the surface per unit time eventually approaches zero. At this moment, pulse cycle is ceased and changed to a purge cycle that removes unreacted precursors and reaction by-products. Surface groups formed by the first precursor are active for second precursor, and therefore next pulse cycle provides new self-terminating chemical reaction. Reactor chamber is normally heated to a certain temperature in order to assure sufficient reactivity of precursors, avoid their condensation, decomposition, or desorption. Such an operation with increased temperature is called thermal ALD and throughout this thesis we will concentrate on this type of ALD.

In comparison to alternative deposition methods, distinctive features of ALD are the very high uniformity of deposited films and control of thickness across the sample with nm-accuracy. For this reason, ALD is widely used for various optical coatings [4]. At the same time, ALD is a perfect method to create a mask on a sample with corrugated surface, where it provides coating with remarkably better conformality than e.g. standard spin-coating of photoresist (Fig. 2.9(b)). Another advantage of ALD is that the processes can be run at relatively low temperatures. These
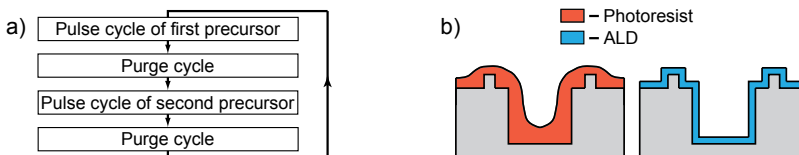

Figure 2.9. (a) Schematic diagram of one ALD cycle and (b) comparison of coverage uniformity when irregular substrate is covered by photoresist or by ALD.

factors make ALD a unique method for accurate deposition of thin layers for nanofabrication and optical applications. The drawbacks of ALD are the very low deposition speed and the overall complexity of equipment.

2.4.2 Al_2O_3 films

Growth of aluminum oxide (Al_2O_3) films is one of canonic and most established ALD processes [39]. Typically, trimethylaluminum ($Al(CH_3)_3$) and water (H_2O) are used as precursors, giving the following process reaction [39, 40]:

$$2Al(CH_3)_3 + 3H_2O \longrightarrow Al_2O_3 + 6CH_4. \tag{2.1}$$
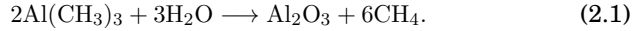
The process is very stable and it can be run within a very wide temperature range from at least 33°C to 300°C [39, 41].

In silicon microfabrication, Al_2O_3 has gained a huge popularity as a mask material in dry etching. The reason is that Al_2O_3 can have close to zero etch rate e.g. when etched in cryogenic ICP-RIE with fluorine-based gas mixtures. Consequently, it provides a unique selectivity of 1:70000 [42] and only a 6-10-nm-thick Al_2O_3 layer enables through-wafer etching of silicon. In addition, Al_2O_3 films are also known for their good mechanical properties [43]. The combination of etch-stopping behavior and mechanical robustness enables to use Al_2O_3 for fabrication of nm-thin released structures [44]. In this thesis, we examine the application of ALD Al_2O_3 films for the fabrication of suspended nanostructures [Publication II].

2.4.3 TiO_2 films

Atomic layer deposition of titanium dioxide (TiO_2) is a less stable process than Al_2O_3 growth. One reason is that the structure of TiO_2 changes depending on the deposition temperature [45]. At lower temperatures TiO_2 grows in amorphous form, while at higher temperatures it grows in polycrystalline form. Considered ALD process employs titanium tetrachloride ($TiCl_4$) and H_2O precursors [46]:

$$TiCl_4 + 2H_2O \longrightarrow TiO_2 + 4HCl, \tag{2.2}$$
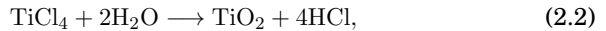
For the particular etching processes considered in this work, the etch-stop properties of TiO_2 are significantly poorer than of Al_2O_3 [47]. Nevertheless, in certain cases TiO_2 can also serve as a mask material in dry etching. In addition, TiO_2 is a high refractive index material that has multiple optical applications, including narrow-bandpass filters and antireflective

coatings [48]. Due to the conformality of ALD growth, thin TiO_2 films can be applied on top of optical components to form overlayers with a shape that resembles the substrate profile. Such overlayers are often utilized to modify light transmission in photonic waveguides [49] and resonant structures [50].

Optical properties of deposited TiO_2 film are largely defined by its crystal structure. Amorphous TiO_2 is generally beneficial due to smaller surface roughness and absence of scattering on polycrystalline grain boundaries. Deposition of amorphous TiO_2 overlayer usually does not lead to a strong increase in losses and in some cases it can even minimize them [49].

In this thesis, we consider only amorphous TiO_2, which is grown at rather low temperature of $120°C$. We concentrate on its applications for optical overlayers in photonics [Publication IV,V] and for fabrication of suspended nanostructures [Publication II].

3. Silicon photonics

3.1 Overview

Silicon photonics is devoted to transmission and manipulation of light via integrated optical circuits. Silicon is used as a material for optical medium due to its high purity and transparency in the infrared wavelength range. The main advantage of silicon photonics over electronic circuits is faster data transmission due to the higher speed and larger bandwidths of light signals. Unlike electrons, electromagnetic waves of various wavelengths can propagate through the same waveguide without crosstalk. Other important benefits are the immunity to electromagnetic interference, moderate power consumption, and reduced demand of heat dissipation [51].

Nowadays, silicon photonics is greatly involved in supercomputers and huge data centers for signal transmission and processing. These advances were made possible due to minimized losses when operating within a certain spectral region of low silicon material absorption, known as telecommunication C-band (around 1.55 μm). During the last decade, many leading high-tech companies such as Intel and IBM have invested in silicon photonics. From technological and commercial points of view, the key feature of silicon photonics is its compatibility with standard semiconductor fabrication facilities.

In silicon photonics, integrated optical components are fabricated on silicon-on-insulator (SOI) platform. Unlike in standard silicon wafers for microfabrication, in SOI the upper silicon layer is isolated from the rest of the wafer by silicon dioxide (SiO_2) layer of a certain thickness. The necessity to implement such a buffer layer is dictated by physics of light confinement, which will be thoroughly discussed in this thesis.

17

3.2 Wave optics of light

Light is manifested as electromagnetic radiation propagating in the form of waves with optical frequencies. These frequencies correspond to the wavelength range from 10 nm to 300 μm, which can be subdivided into ultraviolet (UV, 10 nm to 380 nm), visible (380 nm to 760 nm), and infrared (IR, 760 nm to 300 μm) regions. In vacuum, light propagates with the speed of light $c_\text{o}\approx3\cdot10^8$m/s. An optical wave that has a frequency ν and travels in z direction can be described by position- and time-dependent wavefunction $U(z,t)$ as [52]

$$U(z,t) = a(z)\cos(\omega t + \phi(z)), \tag{3.1}$$

where *a(z)* is amplitude, $\phi(z)$ is phase, and $\omega = 2\pi\nu$ is angular frequency.

Figure 3.1 illustrates a plane wave traveling in z direction as a time- and position-dependent periodic function with a temporal period $1/\nu$ and a spatial period λ. Here, we introduce a concept of wavefronts (Fig. 3.1(b)), which represent surfaces where optical wave has a constant phase (wavefronts of a plane wave are assumed to have infinite extension in plane perpendicular to the direction of propagation). These equiphase surfaces are defined by the cosine function in Eq. (3.1) that has a similar phase when its argument changes by an integer multiple of 2π. When light enters a homogeneous and transparent medium with refractive index n, the propagation velocity of wavefronts known as phase velocity is reduced to:

$$c = \frac{c_\text{o}}{n}. \tag{3.2}$$

Since temporal frequency of wave oscillation is unchanged, a smaller phase velocity will result in a reduced wavelength inside the material, given by

$$\lambda = \frac{c}{\nu} = \frac{c_\text{o}}{n\nu} = \frac{\lambda_\text{o}}{n}, \tag{3.3}$$

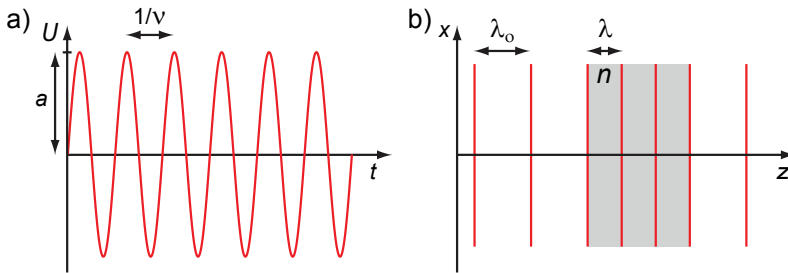where λ_o is a wavelength in vacuum.

Figure 3.1. Plane wave traveling in z direction: (a) temporal dependence of wavefunction and (b) spatial propagation of wavefronts (gray area represents material of higher refractive index).

3.3 Propagation, focusing, and confinement of light

Plane waves described earlier are the theoretical idealization and in reality light propagates in a different form. Most light sources that produce signals for long-distance transmission generate fine light beams of a shape that can be generally approximated by a Gaussian beam [53]. The key property of such a beam is its natural diffraction spreading or divergence, and therefore when a Gaussian beam propagates through a homogeneous medium, it will inevitably increase in size.

Figure 3.2(a) schematically illustrates the evolution of Gaussian beam wavefronts during propagation. A beam emitted by a light source has a finite transverse extension with a bell-shaped intensity profile shown for plane A. Initially collimated beam starts to spread as it propagates (finite length of the wavefronts shown in the Figs. 3.2(a,b) corresponds to the beam size). Divergence is stronger with the smaller aperture defining the initial beam size. It therefore brings a fundamental problem that it is impossible to transfer light through homogeneous medium for long distances in a form of compact beam.
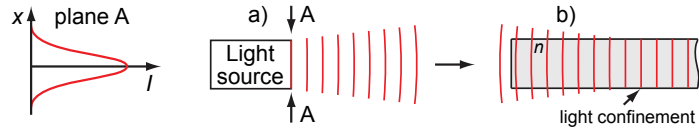
Figure 3.2. Gaussian beam: (a) spreading upon propagation in free-space and (b) focusing by a piece of dielectric material with refractive index n.

The situation with light divergence is completely different when a rod or a slab of higher refractive index material n is installed on the path of propagating light (Fig. 3.2(b)). Since electromagnetic field is a continuous function with respect to spatial coordinates, phase is also continuous and therefore such a rod or a slab will reduce phase velocity in the center of wavefronts, according to Eq. (3.2) [54]. As a result, when the beam travels through a higher refractive index material, its natural diffraction spreading will be counteracted by the reduced phase velocity of the central beam part, providing a continuous focusing effect. For relatively small rods or slabs, beam diameter will typically first shrink and then achieve a balance between divergence and focusing.

If a refractive index contrast between a piece of dielectric material and surrounding medium is high enough, a light beam shone onto this material will be reliably trapped inside. This effect is known as light confinement

and it constitutes the basic principle of light guiding in dielectric waveguides. In nature, the same phenomenon occurs when light is shone e.g. into water jet, which provides light guiding [55] since water is a more optically dense medium than air. Figure 3.3 illustrates a light confinement experiment with three water jets, which appear to be of different colors not because they are dyed fluids, but because they are illuminated by lasers of different colors (wavelengths).
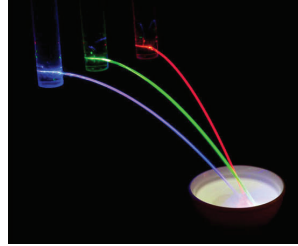
Figure 3.3. Confinement of laser light of different wavelengths in water jets [56].

3.4 Photonic nanostrip waveguides

3.4.1 Modes and polarization

Silicon nanostrip waveguides are the key elements of photonic integrated circuits that are used for component interconnection and data transmission across the chip. Similarly to water jet, light is confined in nanostrip waveguides due to the refractive index contrast between silicon waveguide and surrounding silicon dioxide of lower refractive index. Light propagates through photonic waveguides in a form of guided eigenmodes. For each signal wavelength, a waveguide supports only a finite number of guided modes [57].

The number of supported eigenmodes and their spatial distribution is defined by the waveguide cross section [58]. In general, large waveguides with high refractive index contrast support more modes, and vice versa. Consequently, a small enough waveguide will support only one mode known as fundamental mode for each of two orthogonal polarizations (planes of electric field vector oscillations). Throughout this dissertation, we will consider only fundamental modes.

Structure of standard photonic nanostrip waveguide is shown by a 3D layout in Fig. 3.4(a). Light is guided in z direction through silicon core, which
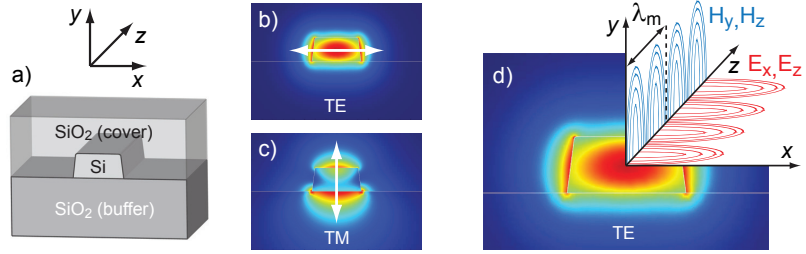
Figure 3.4. (a) Geometry of photonic nanostrip waveguide. (b,c) Comparison of power flow distributions in longitudinal direction shown within *x-y* plane for two polarizations (arrows indicate the plane of electric field vector oscillation). (d) Distribution of power flow in longitudinal direction combined with the structure of electromagnetic field of quasi-TE mode shown for one quarter of waveguide.

has a height of 220 nm and a width of 460 nm. The core is surrounded by SiO_2 protective cover layer (seen as semi-transparent) and SiO_2 buffer layer preventing the leakage of signal. According to the commonly used abbreviations, *x* and *y* axes give the directions of the two orthogonal polarizations of fundamental mode. The mode is said to be TE-polarized when the electric field vector oscillates in *x-z* plane and TM-polarized when it oscillates in *y-z* plane. Figures 3.4(b,c) show the differences in distribution of power flow of TE and TM modes (similar images can be obtained by taking a snapshot at the waveguide facet with highly-sensitive camera). Due to the asymmetric cross section of silicon core, TE mode traverses through more of silicon material than TM mode. Consequently, it experiences a stronger optical confinement and has a more compact field distribution.

A strong Si–SiO_2 refractive index contrast in silicon nanostrip waveguides results in a very complex structure of electromagnetic field. Figure 3.4(d) schematically illustrates the field of TE-polarized mode within one quarter of a waveguide by the electric and magnetic field lines, which are tangential to the local direction of vector field and have a density proportional to the local amplitude of the field. The mode profiles essentially differ from a plane wave, as they contain both transverse (E_x) and longitudinal (E_z) components that are common for hybrid waves. Strictly speaking, polarization state is not uniform across the waveguide cross section. It is linear in the mode center where E_z is zero, and it is elliptical with a plane of polarization ellipse laying in *x-z* plane when estimated with an offset from the center in transverse direction [58]. For this reason, in this dissertation I use abbreviations "quasi-TE" and "quasi-TM" modes to account for nonzero longitudinal components of electric field. Since many authors omit this aspect, in all figures I will label polarizations just as TE

and TM for simplicity.

Propagation of light mode is generally characterized by the parameter known as propagation constant β, which shows the increase in phase angle per unit length. Value of β depends on the distance between two consecutive in-phase oscillations of electromagnetic field (indicated as λ_{m} in Fig. 3.4(d)), and it can be analytically expressed as [64]

$$\beta = \frac{2\pi}{\lambda_{\mathrm{m}}} = k_{\mathrm{o}} n_{\mathrm{eff}}, \tag{3.4}$$

where n_{eff} is effective refractive index of propagating mode and $k_{\mathrm{o}} = 2\pi/\lambda_{\mathrm{o}}$ is a wavenumber in vacuum. Physically, each propagating mode has its own unique β (and n_{eff}) that corresponds to a certain field distribution. Numerically, n_{eff} has a value between the refractive index of the core and of the surrounding medium, and it directly depends on the refractive index profile of the waveguide cross section. In most cases, nanophotonic waveguides have strongly asymmetric structures and the values of propagation constants for two orthogonal polarizations are significantly different. This phenomenon is attributed as birefringence, and it makes a waveguide exhibit different properties when guiding quasi-TE and quasi-TM modes.

3.4.2   Dispersion and its role for nonlinearities

Dispersion can be defined as frequency dependence of propagation constant β, which makes each spectral component acquire specific frequency-dependent phase shift. One way to represent $\beta(\omega)$ is to expand it in a Taylor series about arbitrarily selected frequency ω_0 in the form [59]:

$$\beta(\omega) = \beta_0 + \beta_1(\omega - \omega_0) + \frac{1}{2}\beta_2(\omega - \omega_0)^2 + ..., \tag{3.5}$$

where the derivatives of i-th order are defined as

$$\beta_i = \left(\frac{d^i \beta}{d\omega^i} \right)_{\omega=\omega_0}. \tag{3.6}$$

Second derivative β_2 is abbreviated as group velocity dispersion (GVD) parameter and is expressed in ps^2/m. Physically, β_2 determines how much a light pulse with various frequency components would broaden during its propagation through the waveguide.

Dispersion can be generally divided into two different types, known as material and waveguide dispersion. The source of material dispersion is a wavelength dependence of the refractive index of materials that form a waveguide and its surrounding. Waveguide dispersion is caused by evolution of mode profile with a change of signal wavelength. For example, with

a longer wavelength a signal mode will occupy more space in transverse direction and increase its fraction located outside of silicon core. Consequently, the mode will have modified values of n_{eff} and β, and the dynamics of this change will depend on the waveguide dimensions.

In silicon nanostrip waveguides, waveguide dispersion is very strong due to the high refractive index contrast between silicon core and surrounding SiO_2. Nevertheless, the dispersion-induced broadening of transmitted signals (due to β_2 term) is negligible because of the compact architecture of photonic chips. However, the strong light confinement leads to other types of signal distortion caused by optical nonlinearities due to the enhanced effective nonlinearity parameter [60].

Despite being harmful for signal transmission, optical nonlinearities play a crucial role in on-chip signal conversion [61, 62] and generation of very broadband light [63]. The inherent property of on-chip nonlinearities is that they exhibit large bandwidths already at cm-scale propagation lengths. As a result, dispersion properties of nanostrip waveguides become a factor that limits the performance of on-chip nonlinearities.

Optimization of dispersion maps for nonlinear processes often implies minimization of a phase mismatch $\Delta\phi$, which is expressed as

$$\Delta\phi = \Delta\phi_{NL} + \Delta\phi_L. \tag{3.7}$$

Here, nonlinear part of phase shift $\Delta\phi_{NL} \propto n_2 P$ is defined by the pump power P and the intensity-dependent nonlinear refractive index n_2. Linear part $\Delta\phi_L \approx \beta_2 (\Delta\omega)^2$ corresponds to a dispersion-induced phase shift and its sign depends on the sign of β_2 [64]. Consequently, minimization of phase mismatch requires engineering of dispersion term β_2, which should have a specific negative value that can be adjusted to a particular level of pump power.

Due to its influence on pulse propagation, β_2 is generally used to characterize dispersion properties and regimes. Dispersion is called normal when $\beta_2 > 0$, and anomalous when $\beta_2 < 0$. Figure 3.5 qualitatively shows examples of dispersion curves with their main features. The wavelength where β_2 changes its sign is known as a zero-dispersion wavelength (ZDW). Dispersion characteristics can be very different, within a certain spectral range a waveguide can have one ZDW, two ZDWs (in this thesis abbreviated as ZDW1 and ZDW2), or no ZDW at all (the point of minimal β_2 is then abbreviated as minimum-dispersion wavelength (MDW)).

In silicon nanostrip waveguides, as long as their cross section is relatively large, the total dispersion within the optical C-band is normal ($\beta_2 > 0$) [65],
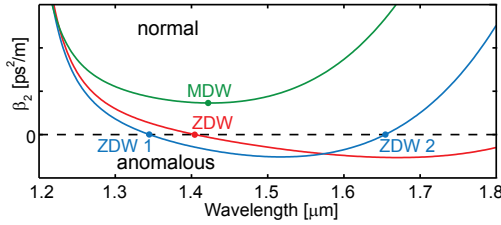
Figure 3.5. Examples of dispersion curves and dispersion regimes.

and it resembles the dispersion of materials forming the structure. When a waveguide cross section is made significantly smaller, the increased contribution of waveguide dispersion counteracts the material dispersion. An alteration of silicon core size is a commonly used technique to modify the dispersion properties. For example, this way the shift of total dispersion to anomalous regime ($\beta_2 < 0$) around 1.55 μm has been experimentally demonstrated [66]. The method has certain drawbacks, which will be discussed in chapter 4.5.1.

An alternative way to engineer dispersion characteristics is to modify the refractive index of the core surrounding. This approach utilizes the effect similar to what is observed in optical fibers when a refractive index change of the core ambient is felt by a propagating signal [67]. This method, however, has not been sufficiently explored in terms of its applications to silicon nanostrip waveguides. In this thesis, we focus on the use of thin dielectric films to realize such a modification of dispersion properties [Publication V].

3.5 Microring resonators

3.5.1 Principle of operation

Optical microring resonators represent fundamental building blocks of photonic integrated circuits. Their applications include optical filters, modulators [68], sensors [69], and on-chip nonlinearities [70].

Figure 3.6 presents a standard configuration of a microring resonator. The resonator is formed by a ring waveguide that is positioned close to the bus waveguide carrying a signal. The two waveguides typically are not in contact. Signal from a straight waveguide is coupled to the ring waveguide via evanescent field when passing the proximity coupler region (shown by a dashed frame in Fig. 3.6). Transmission characteristics of a
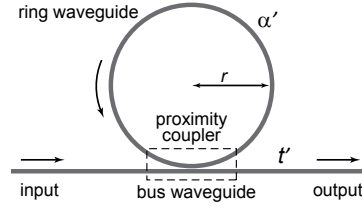
Figure 3.6. Schematic illustration of microring resonator.

ring resonator can be described by the following equation [71]:

$$T(\lambda) = \frac{\alpha'^2 + t'^2 - 2\alpha't'\cos(\theta + \phi(\lambda))}{1 + \alpha'^2 t'^2 - 2\alpha't'\cos(\theta + \phi(\lambda))}, \tag{3.8}$$

where t' is amplitude transmission coefficient of the coupler, α' represents internal losses in the ring per round trip, and the term $(\theta + \phi(\lambda))$ gives a phase factor, where a wavelength-dependent part is defined as

$$\phi(\lambda) = 2\pi \frac{l \, n_{\text{eff}}(\lambda)}{\lambda}. \tag{3.9}$$

Here, n_{eff} stands for the effective index of propagating mode, and l is a physical length of resonator determined by ring radius r.

3.5.2 Parameters and birefringence

In silicon photonics, ring resonators are commonly formed from nanostrip waveguides with asymmetric cross-section and therefore they are strongly polarization-dependent. This property directly reflects in their transmission characteristics and operation parameters.

The main features of typical microring resonator transmission spectra for two input polarizations are illustrated in Fig. 3.7. Resonance dips seen in transmission curves result from destructive interference in the coupling region between input light and signal remaining after one ring round trip. Spacing between two consecutive resonance peaks is abbreviated as free spectral range (FSR), which is wavelength-dependent and can be expressed as:

$$\text{FSR}(\lambda) = \frac{\lambda^2}{l \, n_{\text{g}}(\lambda)}. \tag{3.10}$$

As seen, FSR(λ) depends on the group index n_{g} and takes into account the dispersion properties of a ring resonator as

$$n_{\text{g}}(\lambda) = n_{\text{eff}}(\lambda) - \lambda \frac{dn_{\text{eff}}(\lambda)}{d\lambda}. \tag{3.11}$$

Another key characteristic of resonator is known as extinction ratio of resonance, which characterizes the intensity of resonance peaks. Numerically,
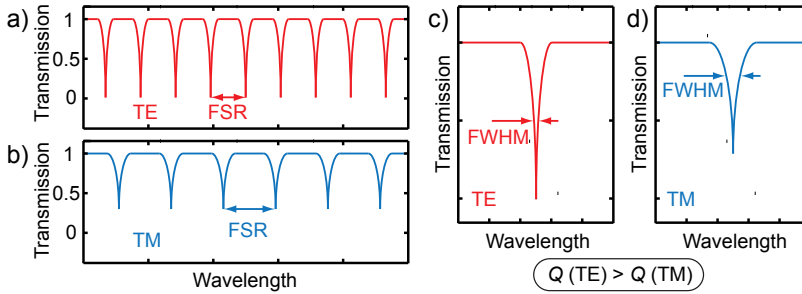
Figure 3.7. (a,b) Typical transmission spectra of microring resonator for two polarizations and (c,d) magnified resonance peaks with indicated full width at half maximum (FWHM).

it corresponds to the difference between on- and off-resonance transmission, expressed in dB or %. The strength of resonance peaks depends on the ratio between resonator internal losses and coupling coefficient, which is generally different for the two polarizations. The peaks are maximized in case of complete destructive interference in proximity coupler, which happens when the fraction of incoming light coupled to the ring is equal to the amount of power lost in the ring during one round trip ($t' = \alpha'$ in Eq. (3.8)). Such operation regime is abbreviated as critical coupling condition or steady state of resonator.

The performance of a resonator can be assessed by the dimensionless parameter known as quality factor Q. Its value is defined by the resonance wavelength related to the full width at half maximum (FWHM, indicated in Fig. 3.7(b)) or $\Delta\lambda$ of the resonance peak:

$$Q = \frac{\lambda_{\mathrm{res}}}{\Delta\lambda}. \tag{3.12}$$

For higher quality factors, resonator losses should be minimized.

As seen in Fig. 3.7, the described parameters (FSR, extinction ratio, quality factor) are generally different for the two polarizations. Such a behavior is called resonator birefringence and it becomes a serious issue for applications where signals have arbitrary polarization (e.g., in telecommunication systems).

A common approach to address birefringence is to implement polarization control or polarization diversity schemes [72]. However, such systems are introduced at the expense of lower signal level, increased noise, and complexity due to the presence of additional components in the system.

On the other side, each of the two orthogonal polarizations has its own distinct advantages and there is a strong interest in ring resonators capable of simultaneously operating with both polarizations. Such ring resonators

are abbreviated as polarization-independent, and they can be utilized for, e.g., sensors with polarization multiplexing [73] or microring resonator filters with doubled free spectral range [74].

The existing solutions to achieve polarization-independent operation employ either a modification of waveguide that forms ring resonator [75, 76], or a change of proximity coupler region [77]. The fundamental limitation of these techniques is that they provide polarization-independent operation only within a narrow bandwidth. In Publication IV, we demonstrate how the application of ALD overlayer can shift the operation of ring resonators towards polarization-independent regime within a broad bandwidth.

3.6 Grating couplers

Photonic grating couplers [78] are used to effectively couple light from optical fiber to a chip at close to the vertical angle. The advantage over alternative structures (such as inverse tapers [79]) is that grating couplers can have arbitrarily defined locations across the chip.

Figure 3.8(a) shows a standard photonic grating coupler that is designed to scatter light upwards from waveguide to optical fiber. Some fraction of input light can be also reflected, scattered downwards, or get transmitted through the grating (not shown in the figure). Lateral dimensions of a grating coupler are usually selected to match the mode field diameter of a single-mode fiber accepting the signal (around 10 μm). At a certain wavelength, standard gratings operate only with one polarization, although there are special designs that simultaneously handle both polarizations [80]. Gratings optimized for the operation within the optical C-band typically have an etch depth of 70 nm and a period of 620 nm. For shorter or longer operation wavelengths, grating period should be reduced
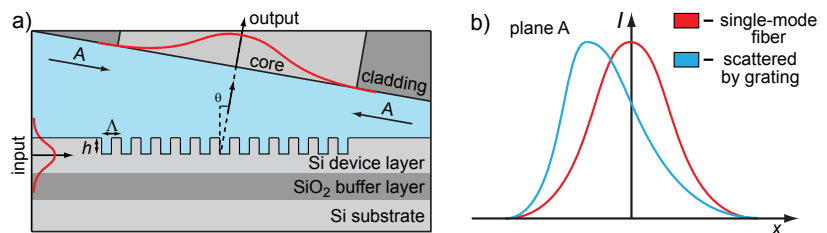

Figure 3.8. (a) Schematic drawing of photonic grating coupler (symmetric) with period Λ and height h of periodic scattering features. (b) Comparison of intensity distribution of electromagnetic field propagating in single mode fiber with the field scattered by grating (shown for plane A indicated by arrows in (a)).

or increased, respectively.

Efficiency of coupling from grating to optical fiber is generally defined by two parameters. First is the fraction of input power scattered upwards by the grating and second is the profile of the scattered field. Typically, the field scattered by symmetric grating has a distribution shown in Fig. 3.8(b). As seen, it is essentially different from close to Gaussian field profile that propagates through a single-mode optical fiber. The reason for such an asymmetric field produced by grating is that each grating groove acts as a scattering center and in symmetric grating the amount of power supplied to more distant grooves (on the right side in Fig. 3.8(a)) is smaller than for the closer grooves. Consequently, the profile of scattered signal has a steep front and a declining tail of lower intensity. This limits the grating performance, since efficient light coupling into a single-mode fiber requires a good match between the two field profiles shown in Fig. 3.8(b), which can be defined by their overlapping integral [58].

There are multiple approaches to improve grating performance. One possible method is to reshape the intensity profile of the scattered field towards Gaussian distribution. In this case, grating strength is varied across the structure with a specially defined distribution. This principle can be realized when either a width [81] or a depth [82] of the grating features (e.g. of grooves) are modulated (Figs. 3.9(a) and (b), respectively). In such non-uniform gratings, the scattering strength varies along the grating and compensates for the decline of power supplied to more distant grooves. From the fabrication point of view, there is a huge difference between the two types of grating modulation. The modulation of groove width (Fig. 3.9(a)) can be accomplished by standard fabrication techniques and therefore the majority of ongoing research employ this modulation type [83]. In contrast, the modulation of depth (Fig. 3.9(b)) is very challenging due to the lack of methods providing arbitrarily defined etch depth across the structure.
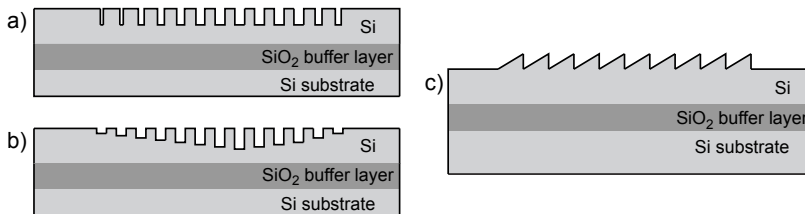

Figure 3.9. Grating with (a) width and (b) depth modulation of rectangular periodic features. (c) Blazed grating.

Another way to improve grating performance is to increase the amount of scattered light. Gratings of special shapes, such as blazed gratings (Fig. 3.9(c)), are known to provide particularly strong light scattering with efficiencies of coupling from waveguide into substrate achieving a value of 97% [84]. Apart from gratings, structures with blazed shapes are widely used in photonic components for focusing and deflection of light, such as integrated Fresnel zone plates [85].

The realization of nanophotonic structures with blazed profiles or varying etch depth requires fabrication methods that can provide accurate height control. In commonly used grayscale lithography [32], the accuracy of height definition is limited by a number of resist gray tones that corresponds to a number of achievable height levels. Limited number of gray tones returns a structure where height is not modulated in a continuous way, but in a discrete way (as a staircase), which has a negative impact on the optical performance. For example, a comparison done in Ref. [86] reveals that approximation of blaze by eight-level staircase structures provides efficiencies of 75% (limited by phase errors), while continuous blazed profiles give efficiencies exceeding 90%. Smooth and almost continuous alteration of height can be realized by FIB milling with virtual 3D patterning maps [87]. Such fabrication, however, is prohibitively slow and expensive to be considered as a feasible mass-fabrication method.

In this thesis, we explore the fabrication technique where the number of gray levels is only limited by the exposure parameters and not by resist characteristics [Publication III]. We will also see that grayscale FIB lithography can be utilized for the fabrication of blazed gratings and multilevel structures with nanoscale resolution.

4. Results

4.1 Nanoparticle gradients through electron beam exposure

Surfaces with molecular gradients are of great importance in nanoscience because they allow for systematic study of different properties as a function of surface density within one compact sample [88]. Gradients of functional molecules provide a cross-functional platform for various types of materials including proteins and nanoparticles, which can be used for molecular transfer and controlled growth of biological material [89].

In this chapter, we consider the fabrication of such gradients through the e-beam exposure of SAMs. The technique provides a fine control over the molecular density across the sample. The method utilizes previously reported observations that patterning of self-assembled thiolate or silane monolayers by e-beam [90] can cause multiple effects: removal, partial removal, disordering, dehydrogenation, crosslinking or change of functional groups.

Figure 4.1 shows the main steps of the proposed process. First, a sample covered with aminosilane-SAM is locally exposed by e-beam lithography. Then, the sample is rinsed with toluene to remove loosely bound silanes
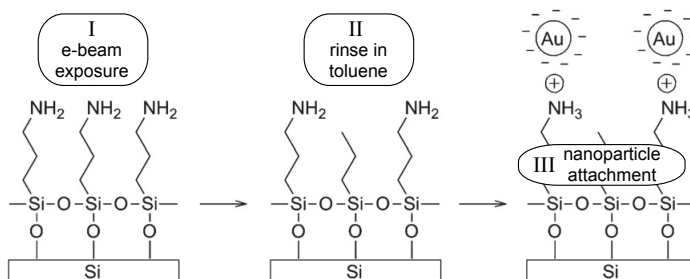

Figure 4.1. Process flow of nanoparticle gradient fabrication [Publication I].

from exposed areas. Finally, the remaining amino groups are subjected to the attachment of negatively charged citrate-stabilized gold (Au) nanoparticles. The nanoparticles are attached in acidic conditions, where amino groups have a positive charge and can attract negatively charged gold nanoparticles [91]. The attachment of nanoparticles is similarly used for visualization of structures by SEM imaging. The detailed protocols and description of utilized materials can be found in Publication I.

Parameters of e-beam lithography were studied and optimized for the preparation of surface gradients of various steepness. The dose-dependent modification of amino-terminated silane was tested for five different acceleration voltages: 1, 3, 6, 9, and 12 kV. The studies were performed by using rectangular patterns of 500 nm by 3000 nm exposed by e-beam with a constant dose across each pattern varying from 20 to 200000 $\mu C/cm^2$. The density of nanoparticles was found to depend on both, e-beam exposure dose and acceleration voltage.

Figure 4.2(a) shows the averaged nanoparticle area density plotted versus the e-beam exposure dose with various acceleration voltages. The number of attached nanoparticles was calculated via software, the mean diameter of Au nanoparticles was estimated to be about 17.4 nm. The smallest dose returned a density of nanoparticles close to the density on untreated surface. The highest dose provided a very low density due to the strong dose-dependent modification of amino-terminated silane layer. The higher the dose, the more silanes are modified and fewer nanoparticles are attached. The range of exposure dose where the major change of nanoparticle
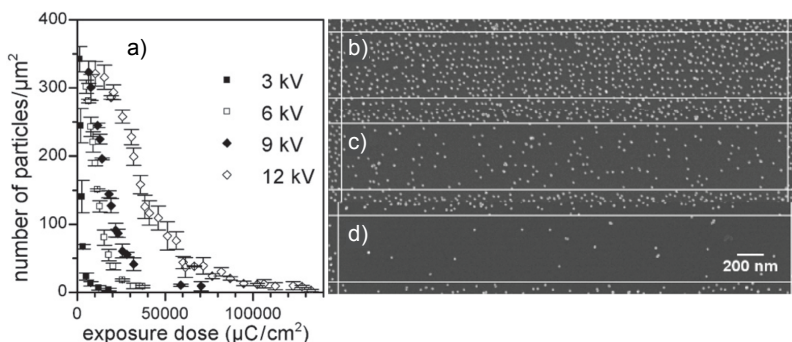
Figure 4.2. (a) Measured nanoparticle area density versus e-beam exposure dose for different acceleration voltages. Error bars indicate the range of measured data for each pattern. (b)-(d) SEM images of patterns written on silanized silicon and subjected to nanoparticle attachment. White lines separate exposed areas from untreated surface. Acceleration voltage was 9 kV for all patterns, dose of exposure was 6400 $\mu C/cm^2$ for (b), 23040 $\mu C/cm^2$ for (c), and 58880 $\mu C/cm^2$ for (d) [Publication I].

density occurs clearly depends on the acceleration voltage. For 1 kV (not shown in Fig. 4.2), electron energies were too small to properly modify the amino-terminated silane surface layer and the particle density never dropped to zero. For all other voltages, the particle density eventually went close to zero, indicating that almost no amino groups were available for nanoparticle attachment.

The identified optimal exposure doses for each acceleration voltage were utilized to fabricate gradients of different steepnesses (Fig. 4.3). The gradients were realized by varying the e-beam exposure dose along 3000-nm-long rectangular patterns. Figures 4.3(b)-(d) show the fabricated gradients written with a 3 kV acceleration voltage. The patterns are extracted from background for clarity, as they are surrounded by a homogeneous layer with high concentration of nanoparticles. Similar gradients were fabricated with other acceleration voltages – 6, 9, and 12 kV. The required exposure time was of the same order for all the voltages, however, the gradients prepared at lower voltages had sharper edges, which complies with the previous report [92]. The presented method thus yields spatial molecular surface gradients with sub-micron dimensions and can be applied to silicon, conductive oxides, and other substrate materials.
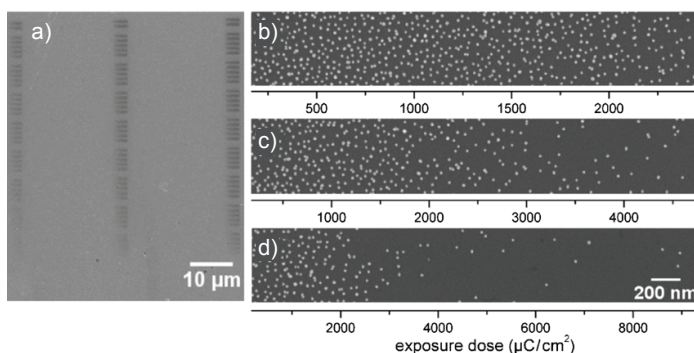

Figure 4.3. (a) General SEM image of gradient patterns written on silanized silicon with 3 kV acceleration voltage without nanoparticle attachment. (b)-(d) SEM images of molecular gradients after attachment of Au nanoparticles. Gradients are of different steepness, dose of exposure increases linearly from left to right and is indicated along the patterns [Publication I].

4.2 Suspended nanostructures on multilevel surfaces

4.2.1 Fabrication method

Suspended nanostructures are of great importance for studies and measurements of thermal conductance [93, 94], thermoelectric properties [95], and radiative enhancement of heat transfer by optical near field [96]. This section considers the integration of such suspended nanonetworks within strongly corrugated surfaces to improve their functionality.

Nanofabrication on samples with strong surface relief presents a great challenge for two reasons. The first one is that it is difficult to uniformly distribute photoresist across the samples with irregular surfaces. The second is a problem of preserving good focusing during the exposure due to small depth of focus (typical for UV and e-beam lithographies).

The proposed fabrication process addresses both of these issues. The problem with nonuniform resist distribution is solved by employing atomic-layer-deposited inorganic resist instead of standard polymer resists (qualitative comparison is shown in Fig. 2.9(b)). Limited depth of focus is circumvented by using FIB as an exposure tool, which has essentially large depth of focus.

Figure 4.4 shows the two modifications of the developed process (sequences (A) and (B)). Both of them provide negative tone patterning, which is beneficial for fabrication of nanostructures surrounded by large empty areas. Sequence (A) employs a single layer TiO_2 resist and sequence (B) employs a bilayer resist (TiO_2 on top of Al_2O_3). Both materials are deposited by ALD at 120°C in the same reactor. TiO_2 acts as a high-contrast negative ion-sensitive resist, following the reported behavior of transition metal oxides [24]. In contrast, Al_2O_3 films irradiated by Ga+ beam work as a positive tone resist [26]. Therefore, in sequence (B) Al_2O_3 is additionally covered by TiO_2 to create the desirable inversion of resist tone. The thick-
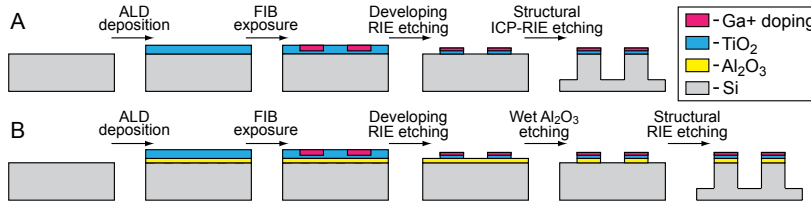

Figure 4.4. Two types of fabrication process: sequence (A) with single layer resist and sequence (B) with bilayer resist.

nesses of ALD films are 50 nm for TiO_2 and 15 nm for Al_2O_3 (TiO_2 film should be thick enough to protect Al_2O_3 from Ga+ ions). FIB patterning is performed with the 30 kV acceleration voltage, the ion beam current of 9.7 pA, and the exposure dose of about 1.5×10^{16} ions/cm^2. Both process sequences employ two dry etching steps. The first is the developing etching that provides a negative tone mask, and the second is the etching that forms final structures.

The main difference between the two sequences is a presence of very robust Al_2O_3 underlayer in (B). This layer defines the type and parameters of applicable structural dry etching. For example, TiO_2 mask is not as robust as Al_2O_3 and in (A) structure should be formed by dry etching with very high selectivity (such as cryogenic ICP-RIE). In (B), Al_2O_3 layer allows for application of etching with lower selectivities, such as room temperature RIE. The achievable minimum feature size is approximately 20 nm for (A) and 35 nm for (B) due to the additional Al_2O_3 wet etching step.

4.2.2 Single layer TiO_2 resist

Figure 4.5 shows the structures with dimensions of different orders of magnitude that were fabricated with a single layer TiO_2 mask. The structure presented in Fig. 4.5(a) almost levitates in air, as underlying silicon walls were thinned and partially removed by etching. Cross and circular shape patterns of TiO_2 mask are well preserved due to very high selectivity of utilized cryogenic ICP-RIE. The etching was performed by an Oxford Plasmalab 100 ICP-Reactive Ion Etcher with the following parameters: process temperature -120°C, SF_6/O_2 gas mixture with the flows of 40/6.5 sccm, respectively, 3 W of forward power and 800 W of ICP power. For these parameters, the experimentally defined value of selectivity was about 1:2000. Therefore, 50-nm-thick TiO_2 mask is sufficient for deep etching
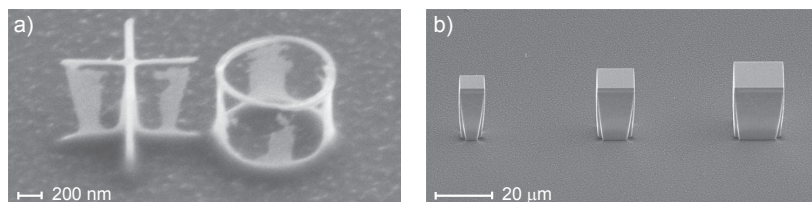

Figure 4.5. (a) Partially released TiO_2 nanopatterns supported by evanescent Si walls. (b) Bulk microstructures for selectivity test. SEM images were taken with a 52 degree angle with respect to surface normal.

required in microfabrication (an example of such microstructure with a height of about 23 μm is given in Fig. 4.5(b)). Consequently, a combination of TiO$_2$ masking and FIB patterning allows for simultaneous micro- and nanofabrication.

Figure 4.6 demonstrates how cryogenic ICP-RIE can be optimized for the fabrication of released nanostructures. Nanopillar arrays shown in the figure represent structures that are commonly used for sensing applications. For both of the shown geometries, the diameter of nanopillar is around 80 nm and the height is about 480 nm. While in Fig. 4.6(a) nanopillars are joined by thin solid walls, in Fig. 4.6(b) they are connected by fine released nanobridges with a width of about 50 nm.
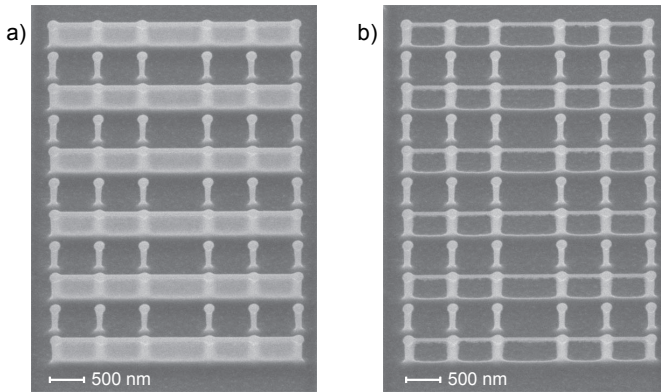
Figure 4.6. Nanopillar arrays joined by (a) thin solid walls and (b) released nanobridges. SEM images were taken with a 45 degree angle with respect to surface normal [Publication II].

The structure seen in Fig. 4.6(a) was formed via close to anisotropic dry etching. The release of nanobridges shown in Fig. 4.6(b) was done through the corresponding adjustment of ICP-RIE parameters. In addition to the change of process temperature and SF$_6$/O$_2$ gas ratio to modify the etching angle, we employed the increase in the concentration of plasma that stimulated the mask undercut. The presented release was realized by increasing the ICP power to 1500 W.

In many cases, suspended nanobridges should follow a sample surface with a strong relief. In these conditions, formation of suspended structures on inclined walls becomes one of the most challenging types of nanofabrication. Such a process implies patterning, developing, and release etching steps to be insensitive to height variation. Here, we demonstrate that the proposed sequence (A) can be applied to tolerate non-planar multilevel sample surfaces, since both resist development and release etching steps

are performed by dry etching.

Figure 4.7 shows an example of nanobridges that are patterned across the inclined wall. The wall forms approximately a 55 degree angle with respect to the top and bottom levels. The presented extract is cut out from the larger SEM image for clarity, the front and the rear edges are the projection of line perpendicular to the wall basement. The difference in height between the upper and lower level is about 12 μm and the nanobridges are approximately 55-nm-wide. The main achievement here is that nanobridges retain their width from the top to the bottom due to the optimization of dry etching parameters, which provides a good uniformity of etching speed across the slope.
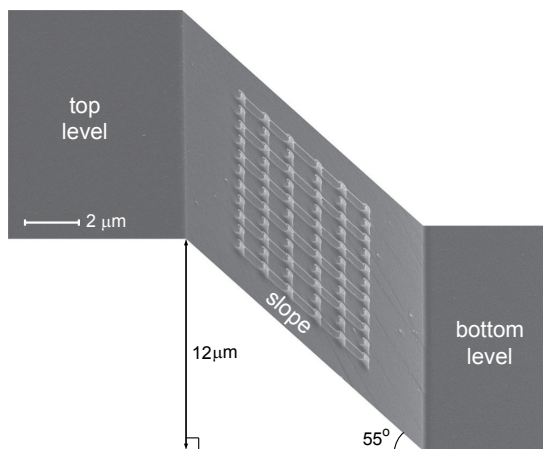
Figure 4.7. Array of suspended nanobridges patterned on inclined wall. SEM image was taken with a 40 degree angle with respect to surface normal.

4.2.3 Bilayer TiO$_2$/Al$_2$O$_3$ resist

Excellent mechanical and etch-stop properties of Al$_2$O$_3$ make it a suitable material for suspended nanostructures. We apply the process sequence (B) with TiO$_2$/Al$_2$O$_3$ bilayer resist to fabricate suspended nanowires of different configurations. Due to the robust Al$_2$O$_3$ underlayer, the sequence (B) enables the dry release by room temperature RIE with flexibly defined parameters. The advantage of RIE in comparison to ICP-RIE is that it can be tuned to very low etching rates, which improves the accuracy and repeatability of the process. The described released structures were obtained by etching in an Oxford Plasmalab 80 Reactive Ion Etcher with lower anisotropy. Such etching removes a large part of TiO$_2$ mask upper layer and leaves predominantly Al$_2$O$_3$ as a nanowire material. Consequently,

it allows for the fabrication of very long and durable few-nm-thick and tens-of-nm-wide suspended nanowire networks.

Figure 4.8 gives examples of different types of suspended nanowires (appear in the image as semitransparent stripes). Figures 4.8(a,b) show a comparison between nanowire geometry when they are either supported by pillars or dangle without any support. Figure 4.8(c) shows a structure of mask and pillars with the higher magnification. All presented nanowires are approximately 15-nm-thick, their width is 40 nm in Figs. 4.8(a,c) and 60 nm in Fig. 4.8(b). The nanowires are very robust, even when their length approaches 4 μm (Fig. 4.8(b)), they do not brake or collapse (the observable whipping is caused by SEM imaging). Therefore, such nanowires also provide a platform for consequent deposition of other materials.
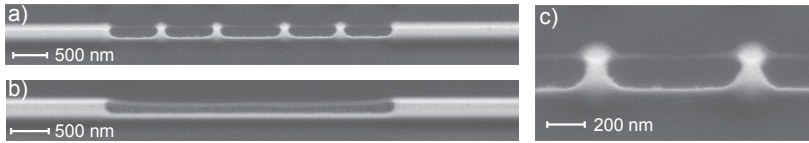
Figure 4.8. Different configurations of suspended nanowires formed with the bilayer resist (sequence (B)). SEM images (a, c) were taken with a 45 degree, and (b) - with a 52 degree angle with respect to surface normal.

4.3 High resolution grayscale lithography

4.3.1 Optimization of etch profiles

This section describes the realization of grayscale lithography for nanophotonics by FIB exposure of inorganic resist. Grayscale lithography is used for fabrication of features with arbitrarily-shaped surface profiles by varying the exposure dose across the sample (discussed in section 2.2.3).

Figure 4.9 shows the process flow of the developed lithography, which contains three main steps: resist deposition, FIB exposure, and dry etching that forms the structure. The number of process steps is minimized because the resist development and the formation of final structure are done simultaneously (in contrast to typical process flow illustrated in Fig. 2.5). Silicon nitride (Si_3N_4) inorganic resist is deposited at 770°C by low pressure chemical vapor deposition. FIB exposure is performed with the acceleration voltage of 30 kV and the ion beam current of 9.7 pA, which provides high resolution, fast exposure, and Ga+ penetration depth of about 30-35 nm [20, 30]. The thickness of Si_3N_4 resist layer is set to

Figure 4.9. Process flow of grayscale FIB lithography. (d) Deposited resist is exposed by linearly varying dose indicated in (c). Formed structure (e) has different height when etching is performed with low (h_1) or high (h_2) selectivity.
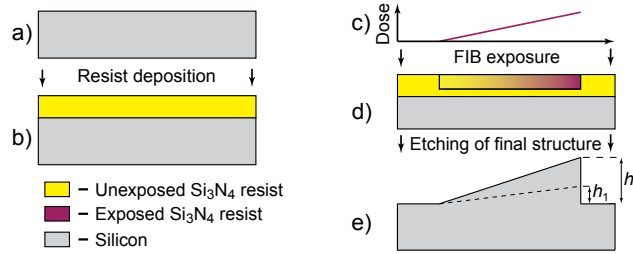
50 nm to be sufficient to accumulate ions and protect underlaying silicon from FIB irradiation. During the exposure, Si_3N_4 resist receives different amount of implanted ions at different locations. Consequently, it provides different masking properties across the structure that return a particular height profile of the structure formed by dry etching. Patterns written by FIB in Si_3N_4 resist are etched in RIE with fluorine-based chemistry, where they exhibit etch-retarding behavior due to the formation of nonvolatile GaF_x masking compound on Ga+-irradiated areas [29, 30].

For the best control of surface profile in grayscale FIBL, the height of final structure should be linearly dependent from the exposure dose. In practice, it is very challenging to achieve due to the trade-offs between surface smoothness, etching selectivity, and anisotropy. Smooth and defectless surface is a prerequisite for good optical performance of fabricated components, while anisotropic etching is needed to ensure high lateral resolution. Selectivity should be adjusted to particular exposure parameters and provide the required height of formed structure.

Figures 4.10(b-d) show the possible problems that occur during the dry etching of patterns written by FIB with a linearly varying dose (Fig. 4.10(a)). An ideal grayscale profile should have a linearly increasing feature height, as illustrated in Fig. 4.9(e). In reality, the process can be ruined if, e.g., the mask peels off due to poor anisotropy and very high selectivity, as shown in Fig. 4.10(b)). Alternatively, the regions of smaller exposure dose can be severely damaged in case of highly anisotropic etching with intensive surface passivation (Fig. 4.10(c)). Even when reasonable surface quality is achieved, rising up slope in the graytone region can have strongly nonlinear profile (Fig. 4.10(d)), which results in a poor overall height control. All SEM images presented in this section were taken with a 52 degree angle with respect to surface normal.

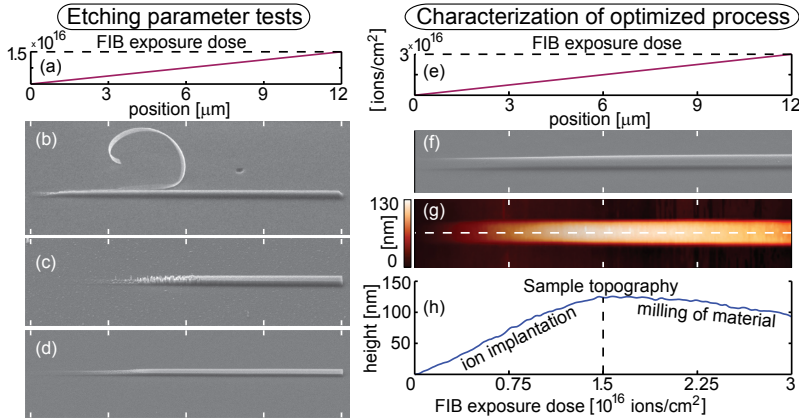The optimized parameters for etching in Oxford Plasmalab 80 Reactive

Figure 4.10. Left: (b-d) SEM images of possible issues during RIE of patterns written with linearly varying dose (a). Right: optimized process. Stripe pattern is written with linearly varying FIB dose (e) and etched by anisotropic RIE (SEM image (f)). (g) Topography characterized by AFM and (h) the corresponding height profile measured along the white dashed line. Reproduced with permission from [Publication III]. Copyright 2014, AIP Publishing LLC.

Ion Etcher provided smooth sample surface, high anisotropy, and close to linear dependence of feature height from the masking dose. This etching employs pure CF_4 gas with the flow of 50 sccm, RF power of about 100 W, and process pressure from 100 to 250 mTorr (is varied for selectivity adjustment).

As seen in Figs. 4.10(f,g,h), there is almost a linear height-to-dose correlation until the dose exceeds 1.5×10^{16} ions/cm^2. Above this dose, FIB-induced sputtering of material becomes very intensive, it overweights the masking effect in RIE and decreases the final structure height.

4.3.2 Grating with varying modulation depth

The optimized process was applied to fabricate structures with a fine increment of gray levels. Figure 4.11 shows a structure obtained by incorporation of linearly varying modulation depth into the profile of a binary grating. The level of each groove (and rib) is defined individually. The number of gray levels is only limited by the exposure parameters and not by the resist characteristics (in contrast to standard optical and e-beam grayscale lithographies). In practice, it means that a few thousand gray levels can be defined during patterning by standard FIB systems with a 16 bit digital-to-analog converter.
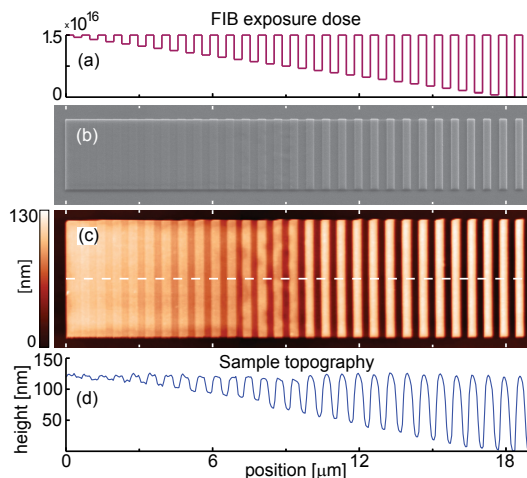
Figure 4.11. Linearly varying modulation depth applied to binary grating (period is 650 nm and height is 125 nm). (a) Profile of FIB exposure dose, (b) SEM image, (c) characterization of topography by AFM and (d) the corresponding height profile measured along the white dashed line. Reproduced with permission from [Publication III]. Copyright 2014, AIP Publishing LLC.

4.3.3 Blazed grating with varying slope angle

When the exposure dose is spatially varied within small areas, the proposed lithography allows for fabrication of structures with complex pre-designed profiles. An illustrative example of such structures is a blazed grating with a varying angle of blaze along the grating and a very small period. Figure 4.12 shows two gratings with periods of 200 nm and 150 nm where the blaze angle is modulated, starting from steep slopes near the edges and decreasing towards the center. Fabrication of such fine gratings is possible due to the small proximity effects and limited penetration depth of ions into inorganic resist. Grating with a period of 200 nm (Fig. 4.12(a)) exhibits features that clearly reflect the applied dose. The period of 150 nm (Fig. 4.12(b)) is the smallest period for utilized parameters when blazed grating profiles can be reliably patterned. Further reduction of period causes a significant degradation of blaze profiles. Fabrication of presented blazed gratings with alternative grayscale lithographies (e.g., e-beam lithography) is very complicated and has not been realized so far. If the same grating structures were fabricated by standard FIB milling, there would be a vast increase in FIB processing time (hours instead of tens of seconds).

The ratio between etching rates of inorganic resist irradiated by FIB and non-irradiated resist, known as selectivity, acts as a measure of contrast
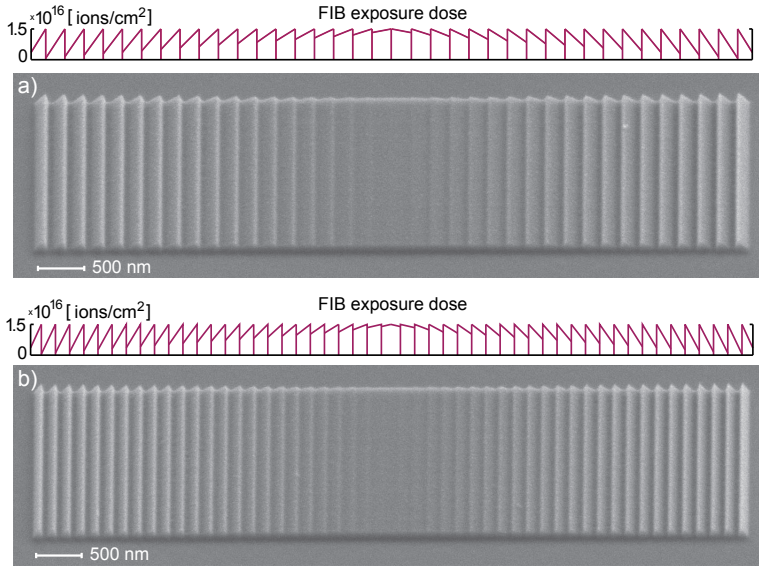
Figure 4.12. SEM images of blazed gratings with varying blaze angle along the structure: (a) period 200 nm and height 140 nm, (b) period 150 nm and height 140 nm. Profiles of FIB exposure dose are indicated above each grating.

in the considered process. Consequently, the achievable height of final structure is defined by the selectivity of utilized etching. Figure 4.13 shows three gratings fabricated with the corresponding adjustment of RIE process to the low (Fig. 4.13(a)), middle (Fig. 4.13(b)), and high (Fig. 4.13(c)) selectivity. The high selectivity conditions enabled the fabrication of a grating with the 200 nm period, 200 nm height, and very steep sidewalls with angles of inclination exceeding 60 degrees. The maximum achievable feature height is limited because further increase of structure height requires shifting the process to even higher selectivity that will in turn promote defect formation and increase overall roughness due to uneven mask removal.
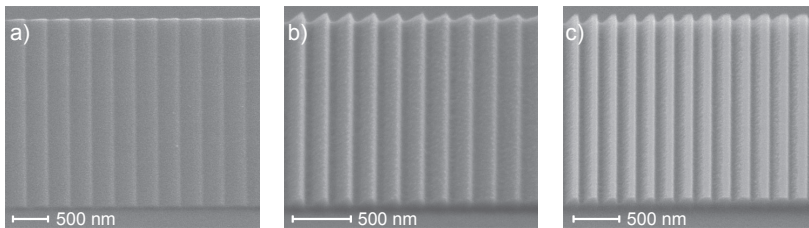
Figure 4.13. SEM images of blazed gratings etched with different selectivity: (a) height is 70 nm, (b) height is 140 nm, (c) height is 200 nm.

4.4 Modification of ring resonator operation by ALD

4.4.1 Chip design for local ALD deposition

In this section, we show that the local deposition of thin ALD overlayer can be used to modify transmission characteristics of ring resonators and simultaneously preserve their broad-bandwidth operation. The experimental study was carried out with specially designed photonic chips (Fig. 4.14) patterned by 248 nm deep ultraviolet lithography. Each chip contained ring resonators with a 50 μm radius and a 300 nm gap between the ring and the bus waveguides. The resonators were formed from nanostrip waveguides of 220 nm height and 460 nm width. Input and output waveguides were terminated by inverse tapers at the chip facets. This allows for efficient coupling of light with minimized wavelength dependence via tapered optical fibers.

Initially, the whole chip surface was covered with SiO_2 protective cover layer (cross section A in Fig. 4.14). Later, at the specific locations of ring resonators, the cover layer was removed by highly selective dry etching. As a result, the ring resonators were completely exposed to ambient, while the rest of the chip surface remained protected. Such a design enables the local deposition of ALD films only onto the ring resonators (the structure covered by ALD overlayer is illustrated by the cross section B in Fig. 4.14). The deposition of ALD TiO_2 overlayers was performed via $TiCl_4/H_2O$ process at 120°C in Beneq TFS 500 reactor.
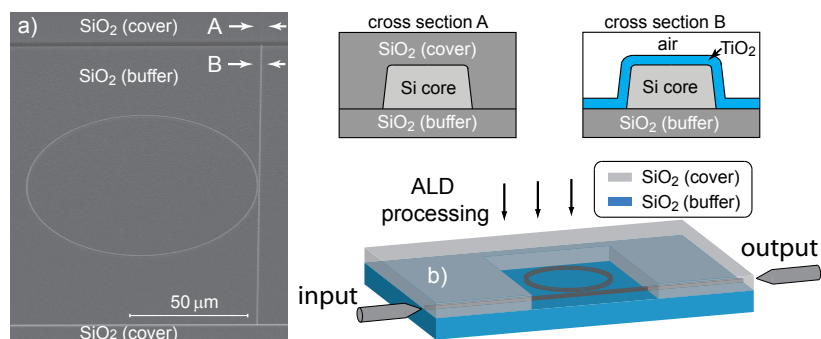

Figure 4.14. (a) SEM image of ring resonator design utilized in experiments taken with a 52 degree angle with respect to surface normal. Schematic cross sections A and B correspond to the locations indicated in SEM image. (b) Structure layout of chip with ring resonator: protective SiO_2 layer is removed from resonator, light is coupled through the chip facets.

4.4.2 Coupling regimes and quality factors

We first consider how the deposition of an ALD film physically modifies the geometry of the ring resonators. As shown in Figs. 4.15(a-d), the application of overlayer increases the waveguide cross section and narrows down the gap between the ring and the bus waveguides in the proximity coupler region. It also changes the profiles of propagating modes of both polarizations, which is illustrated by simulations in Figs. 4.15(e-l). As seen, TiO_2 overlayer causes stronger modifications for quasi-TM mode profiles.
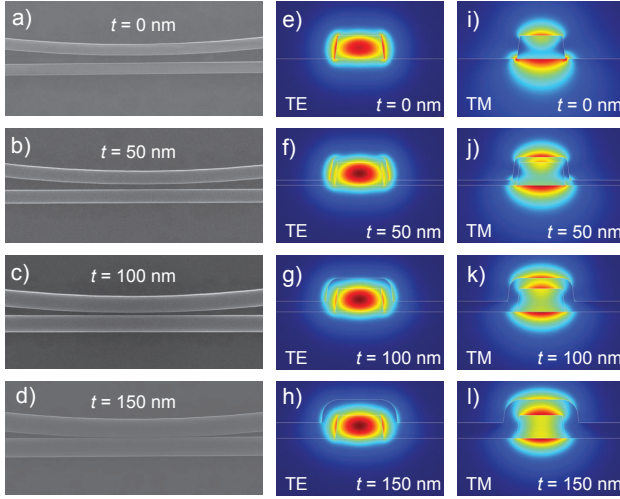
Figure 4.15. (a-d) SEM images of ring resonator proximity couplers, (e-l) simulated field distributions of fundamental modes for different thicknesses t of TiO_2 overlayer.

The change of resonator coupler region and mode profiles results in modification of resonator coupling coefficient. This coefficient has the main influence on resonator transmission characteristics, since the waveguide bending losses are small due to the large 50 μm resonator radius. We studied the transmission spectra of ring resonators covered with TiO_2 films of different thicknesses varying from 0 to 250 nm. The samples were characterized by superluminescent LED source (with a center wavelength at 1570 nm and a bandwidth of 100 nm) and an optical spectrum analyzer, input polarization was controlled by fiber polarizers and polarization maintaining fibers.

Figures 4.16(a-j) present the obtained ring resonator transmission spectra for two orthogonal polarizations and various TiO_2 thicknesses. The resonance peaks have a maximum strength in a critical coupling regime. When the coupling between the ring and the bus waveguides is weaker,

resonator is undercoupled, whereas with a stronger coupling resonator is overcoupled. As seen in Figs. 4.16(a,f), the uncoated samples exhibit weak resonances because of the weak coupling given by the large 300 nm gap. The addition of ALD layer increases the coupling for both polarizations and when the thickness approaches 100 nm, the ring resonators operate close to the critical coupling regime for quasi-TM mode (is seen from the strong transmission dips in Fig. 4.16(h)). Quasi-TE mode is less sensitive to overlayer deposition and it achieves the critical coupling only with a 150-nm-thick ALD layer (Fig. 4.16(d)). At this point, quasi-TM polarized mode is already overcoupled and detuned from the strongest resonances (Fig. 4.16(i)). When the thickness of the TiO_2 layer exceeds 150 nm, quasi-TE mode does not see much of a change in waveguide surrounding, and further increase of TiO_2 thickness gives only a minor spectrum change. It is important that even thick TiO_2 overlayers do not promote periodic beating of coupling coefficient [97, 98] and resonators retain the broad-bandwidth operation.

The different character of transmission spectra evolution for quasi-TE and quasi-TM modes is reflected in the ring resonator operation param-

Table 1

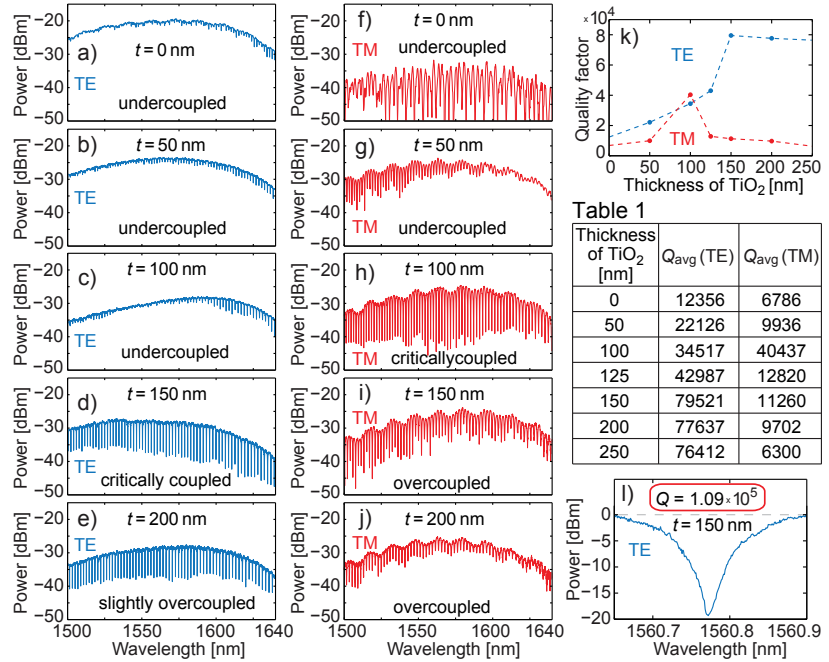| Thickness of TiO_2 [nm]	Q_{avg} (TE)	Q_{avg} (TM)
0	12356	6786
50	22126	9936
100	34517	40437
125	42987	12820
150	79521	11260
200	77637	9702
250	76412	6300

Figure 4.16. (a-j) Transmission spectra of ring resonators with TiO_2 overlayers of various thicknesses t. Plot (k) and Table 1 present the average values of quality factors calculated from the transmission spectra. (l) Example of high Q resonance peak.

eters. We characterize the differences in performance by calculating the average values of quality factors within the considered wavelength range. The data are presented in numerical (Table 1 in Fig. 4.16) and graphical form (Fig. 4.16(k)). A trend visible from the plot indicates that the dynamics of Q values corresponds to the variation of resonator extinction ratio. It is valid both for TiO_2 thicknesses when the strongest peaks (and Q values) are observed, and in terms of saturation in change for quasi-TE mode when the TiO_2 thickness exceeds 150 nm. The highest quality factors were measured for quasi-TE mode with a 150 nm ALD overlayer. The Q values exceeded 100 000 within the C-band, an example of such a peak measured by a tunable external cavity laser with 1 pm resolution is shown in Fig. 4.16(l). In order to simultaneously maximize the intensity of resonance peaks and Q factors for both polarizations, one has to provide a particular gap between the ring and the bus waveguides, as quasi-TE and quasi-TM modes evolve differently when ALD layer is added.

4.4.3 Polarization-independent operation

Here, I present the experimental data on how peak-to-peak spacing (FSR) in the resonator transmission spectrum is shifted towards polarization-independent operation. Different sensitivities of quasi-TE and quasi-TM modes to TiO_2 overlayer (and therefore different modifications of effective indices n_{eff}) enable to manipulate the ratio between FSR for the two polarizations. Numerically, it is illustrated by the analytical expression of Eq. (3.10), which accounts for the absolute value and the wavelength dependence of mode effective index.

Figures 4.17(a-d) illustrate the change of FSR wavelength dependence when TiO_2 overlayers of various thicknesses are applied (peak positions were identified by own written Matlab script from the measured transmission spectra). As the change of FSR caused by TiO_2 overlayer is significantly stronger for quasi-TM mode, with a certain TiO_2 thickness (here 150 nm) covered ring resonator exhibits similar peak-to-peak spacings for the two input polarizations (Fig. 4.17(d)). A broad bandwidth operation where the FSRs for the two polarizations are similar is made possible by matching the FSR wavelength dependencies.

Examples of ring-resonator transmission spectra that are tuned towards polarization-independent operation are shown in Fig. 4.17(e). A good match of the peak positions for the two input polarizations is kept within a bandwidth of approximately 100 nm. As also seen, the coupling conditions for
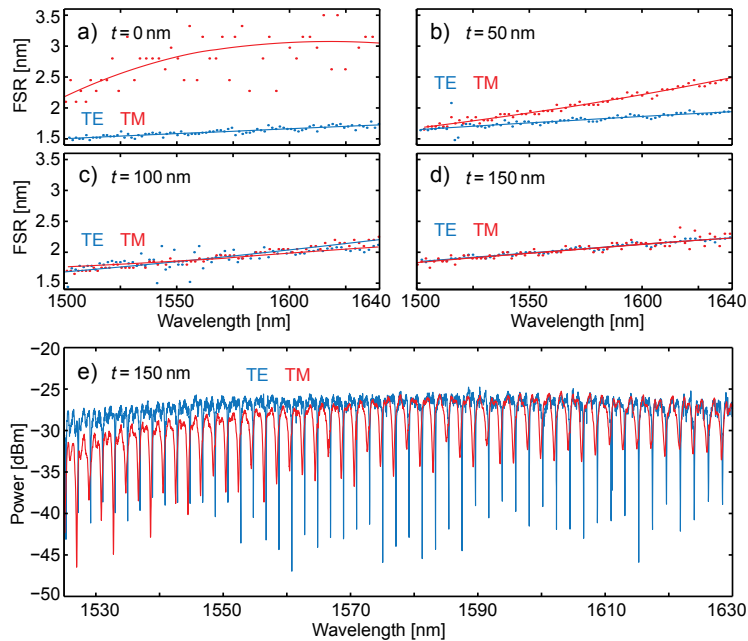
Figure 4.17. (a)-(d) Wavelength dependence of FSR for two input polarizations with TiO_2 overlayer of various thicknesses t. Experimental data (dots) are approximated by a fit (solid lines). (e) Transmission spectra of a ring resonator with 150-nm-thick TiO_2 overlayer [Publication IV].

the quasi-TM mode are not optimal, which results in a gradual reduction of resonance peak strength at longer wavelengths. This issue can be addressed by optimizing the coupling regime for both polarizations through the selection of a suitable waveguide geometry and a specific gap between the bus and the ring waveguides.

4.5 Engineering of nanostrip waveguide dispersion by ALD

4.5.1 Modification of dispersion via waveguide dimensions

In this section, we will look at the optimization of the nanostrip waveguide dispersion properties through the deposition of thin ALD overlayers. We will see that by coating a waveguide with a conformal nm-thick TiO_2 film, one can achieve dispersion characteristics that facilitate specific applications within the telecommunication C-band. Dispersion properties were studied numerically with a computational model built in a commercial full-vectorial finite element method (FEM) solver [99] in a mode analysis mode.

Figure 4.18. (a) FEM model geometry representing cross section of nanostrip waveguide coated by TiO$_2$ overlayer. The parameters are: waveguide height h, waveguide wid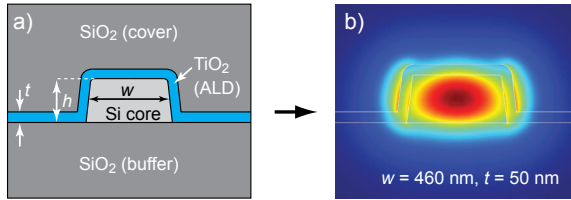th w, and thickness of TiO$_2$ layer t. (b) Example of power flow distribution in longitudinal direction for the fundamental TE mode at 1.55 μm.

Figure 4.18(a) shows the geometry of the utilized FEM model, which represents a cross-section of silicon nanostrip waveguide covered by thin TiO$_2$ layer and SiO$_2$ protective cover layer. The profiles of TiO$_2$ layers were identified from SEM images, the refractive indices of Si and SiO$_2$ were calculated from the corresponding Sellmeier equations [100]. The refractive index of thin TiO$_2$ overlayer was determined from own experimental data (amorphous TiO$_2$ film was deposited onto a silicon substrate at 120°C). The model was used to calculate the field distributions and the propagation constants of the fundamental quasi-TE polarized mode at different wavelengths (an example of the mode profile is shown in Fig. 4.18(b)). Consequently, the model accounts for both waveguide and material dispersion. Obtained values of GVD parameter were verified using the benchmark data provided by [66, 101].

We first consider how the dispersion curves of a standard nanostrip waveguide evolve when the waveguide width is varied and the height has
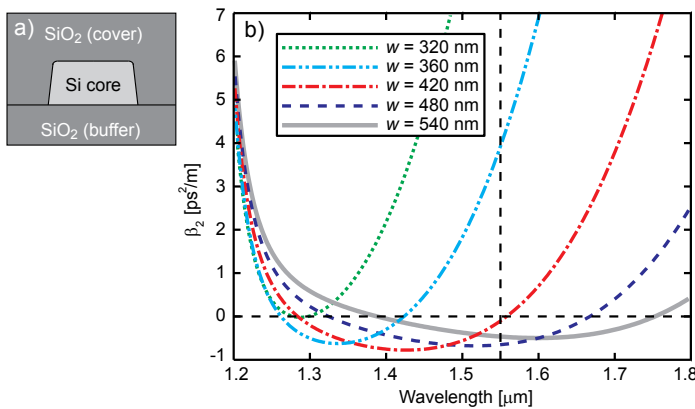

Figure 4.19. (a) Schematic cross-section of simulated waveguide (height is set to 220 nm). (b) Dispersion curves for variable waveguide widths [ⓒ 2012 IEEE, Publication V].

a constant value of 220 nm (Fig. 4.19). Such a modification of waveguide cross section represents a typical case when the height is fixed and cannot be adjusted due to a particular thickness of the SOI device layer. As seen in Fig. 4.19(b), for narrower waveguides ZDW2 shifts towards the shorter wavelengths and for a certain waveguide width (around 420 nm) it falls close to the center of the telecommunication C-band (1.55 μm). At the same time, narrowing of a waveguide increases the slope of the dispersion curve in the proximity of ZDW2.

High dispersion slope near zero-dispersion wavelength is undesirable due to necessity for many nonlinear processes to minimize the phase mismatch (Eq. (3.7)). A strong dispersion slope near ZDW2 makes the dispersion-induced phase shift $\Delta\phi_L$ very sensitive to minor variations in the waveguide geometry. The engineering of dispersion by solely modifying the waveguide width does not provide the desirable moderate dispersion slope around the required ZDW.

4.5.2 Modification of dispersion by ALD

When a waveguide is covered by a thin TiO$_2$ overlayer, it modifies the dispersion profile without changing the dimensions of silicon core. The deposition of high refractive index TiO$_2$ coating changes the refractive index seen by the traveling mode, which modifies the absolute value and the wavelength dependence of the propagation constant β.

Figure 4.20(b) illustrates how TiO$_2$ overlayer of a proper thickness can
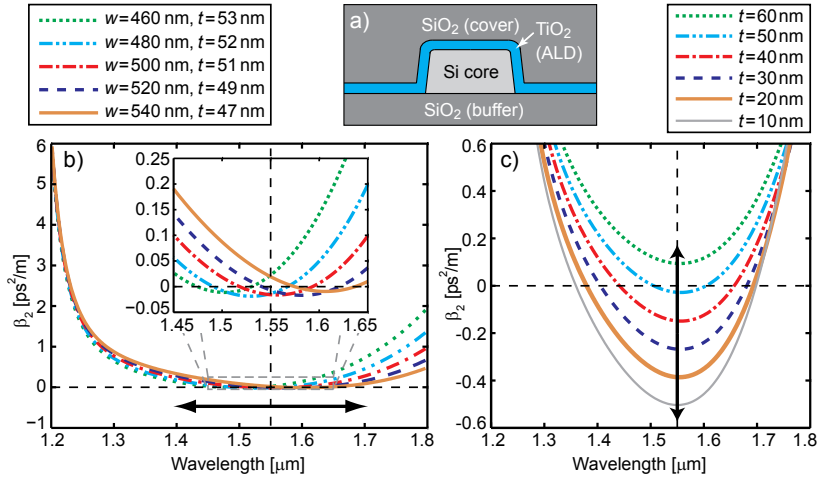
Figure 4.20. (a) Schematic layout of simulated waveguide cross-section. Dispersion curves for (b) variable TiO$_2$ thickness and waveguide width, (c) variable TiO$_2$ thickness and fixed waveguide width of 500 nm [© 2012 IEEE, Publication V].

provide small negative β_2 values across the very broad wavelength range with the corresponding adjustment of the core width. In this case, the slopes of the dispersion curves near the ZDWs remain moderate. In addition, for commonly used wavelengths around 1.55 μm, β_2 can be adjusted to a particular value including the range from large negative numbers to zero (shown in Fig. 4.20(c)). It is realized by setting the waveguide width to a fixed value and varying solely the TiO$_2$ film thickness.

The presented control over β_2 profile shown in Figs. 4.20(b,c) also allows for acquiring both ZDW1 and ZDW2 within the C-band and tuning the wavelength spacing between them. It results in the improved stability of nonlinear phase shift compensation for various power levels (Eq. (3.7)) due to the minimized slope of β_2.

5. Summary and Outlook

The thesis introduced novel nanofabrication practices and extended the range of existing nanotechnology applications, particularly for sensing and integrated optics. The presented research consists of two parts. The first one is focused on nanofabrication and the second describes the modification of photonic devices and waveguides by the deposition of thin films. The three main types of processing utilized in this work are: atomic layer deposition, exposure by focused ion beam, and dry etching. The summary below describes the value of the proposed methods and the examples of their possible applications.

The strategy for patterning of amino-terminated silane layers presented in Publication I gives a way to control molecule surface density with nanometer accuracy. The method can be customized for various materials, as the amino groups can be used for attachment of metals, polymers, carbon nanotubes, fluorescent quantum dots, and biological molecules. The dimensions of patterned areas can achieve centimeter scale with the use of advanced electron beam lithography systems. The untreated surfaces can be made free of functional molecules through the use of additional masks during aminosilane deposition. The substrate material is not limited to silicon and can be extended to multiple conductive oxides, such indium-tin oxide, which gives a huge advantage for sensing applications.

Nanofabrication on multilevel surfaces shown in Publication II is of prime importance for 3D integration, micro- and nanofluidics, and lab-on-a-chip concepts. The process enables to confine, isolate, and manipulate analytes within nanoscale volumes [102]. For example, fabrication of nanopillars within micron-scale channels and grooves can provide a control over wetting behavior through a combination of hydrophobic [10] and hydrophilic [9, 103] properties. When such nanopillars are coated with metals [104], it can significantly enhance the level of signal in sensing and spectroscopy.

In addition, periodic patterns within micron-scale grooves can be utilized for plasmonic resonant structures [105].

Another functionality of the process demonstrated in Publication II was the fabrication of suspended nanowires that can follow the irregular profile of the sample. Normally, suspended nanowires are used in experiments devoted to thermal conductance [93, 94], thermoelectric properties [95], radiative enhancement of heat transfer [96], etc. In this work, suspended nanonetworks were fabricated across the inclined walls of micron-scale groove. As a result, the above mentioned applications can be enriched by micro- and nanofluidics and sensing. The essential advantage of the presented method is that it is fast and reproducible due to the minimized number of process steps. In addition, the approach is not limited to silicon nanofabrication and can be similarly applied to polymers [106].

Publication III shows the realization of the grayscale lithography with simultaneously high lateral and vertical resolution. The process can facilitate fabrication of miniature diffractive optics for extreme ultraviolet and soft X-ray radiation [107]. It can also improve the performance of photonic grating couplers by implementing the asymmetric modulation along the grating [81]. The shown control over the height of fabricated structures allows for mapping of effective refractive index used in gradient-index optics. Consequently, the presented method enables the fabrication of integrated focusing components, such as compact aberration-free Luneburg photonic [108] or plasmonic [35] lenses. The use of substrates with pre-designed surface profiles can be extended by a subsequent metal deposition step. It would allow for unidirectional excitation of surface plasmon waves [109], rainbow trapping [110], or shaping of separate metal film by using the original silicon structure as a mold for 3D stripping [111]. The shown grayscale nanolithography also enables realization of directed motion of liquid based on surface propulsion [112], which is enhanced when a period of ratchet structures achieves sub-micrometer scale [113]. In addition, fluid dynamics can be complemented with nanoscale optofluidic transport [114].

In Publication IV, I showed how the application of atomic layer deposition can tune the optical response of ring resonators towards polarization-independent regime across the broad bandwidth. In this regime, resonators can operate with arbitrarily polarized light and do not require polarization control schemes. With the proper offset between resonant peaks of the two polarizations, the use of cross-polarized light can

double free spectral range of a resonator. It therefore allows for reduction of ring resonator radius and more compact integration (Eq. (3.10)). In addition, the application of thin TiO_2 overlayers gives an opportunity to manipulate resonator coupling coefficients and Q values with high accuracy. The demonstrated approach can be extended to more complicated schemes. Specifically, it can be utilized to control intercoupling coefficients of apodized multiorder microring resonator arrays [115], nonlinearities in ring resonators cascades [70], and microcavity-resonator-based active devices [116].

Publication V introduces a simple and straightforward method to manage the dispersion properties in photonic nanostrip waveguides. It allows for the optimization of on-chip nonlinear processes through the adjustment of zero-dispersion wavelength and flattening of the dispersion curve. The advantages of this approach are that it provides the compensation of fabrication imperfections and multiple samples (photonic chips) can be treated simultaneously. The utilized atomic layer deposition of TiO_2 is a low temperature process, which makes it compatible with the existing silicon photonics platform. The deposition of TiO_2 overlayer can also reduce the propagation losses caused by sidewall roughness of nanowaveguides [49]. Apart from nanostrip waveguides, the presented dispersion management can be applied to other types of nanophotonic waveguides. Nowadays, it is particularly relevant due to the increasing number of alternative fabrication platforms, where waveguides are formed by the deposition of material onto a substrate. Such waveguides (e.g., amorphous silicon waveguides [117]) can have a flexibly defined shape, which can be initially optimized for the known parameters of atomic layer deposition.

The studies presented in this thesis are original and have a showcase character. The scientific value of the presented methods is that they provide principles, which can be extended to other materials and applications. Thus, area density gradients of amino groups presented in Publication I provide means for highly accurate sensing, transport, and growth of various molecules. Suspended nanostructures shown in Publication II can serve as a platform for deposition and characterization of other materials. Grayscale lithography demonstrated in Publication III can assist the research on novel types of focusing and resonant photonic structures, which can not be produced by commonly used grayscale lithographies. Polarization-independent operation of ring resonators shown in Publication IV can be combined with a number of other functions (sensing, thermally or

electrically controlled logic). Finally, the dispersion management presented in Publication V can be further enhanced by the atomic layer deposition of nonlinear nanolaminates [118].

Bibliography

[1] L. Bocquet and E. Charlaix, "Nanofluidics, from bulk to interfaces," *Chem. Soc. Rev.* **39**, 1073–1095 (2010).

[2] C. H. Ahn, K. M. Rabe, and J.-M. Triscone, "Ferroelectricity at the Nanoscale: Local Polarization in Oxide Thin Films and Heterostructures," *Science* **303**, 488–491 (2004).

[3] E. Katz, I. Willner, and J. Wang, "Electroanalytical and Bioelectroanalytical Systems Based on Metal and Semiconductor Nanoparticles," *Electroanal.* **16**, 19–44 (2004).

[4] D. Riihelä, M. Ritala, R. Matero, and M. Leskelä, "Introducing atomic layer epitaxy for the deposition of optical thin films," *Thin Solid Films* **289**, 250–255 (1996).

[5] J. D. Joannopoulos, S. G. Johnson, J. N. Winn, and R. D. Meade, *Photonic Crystals: Molding the Flow of Light* (Princeton University Press, Singapore, 2008), 2nd edition.

[6] L. Grill, M. Dyer, L. Lafferentz, M. Persson, M. V. Peters, and S. Hecht, "Nano-architectures by covalent assembly of molecular building blocks," *Nat. Nanotechnol.* **2**, 687–691 (2007).

[7] O. Ikkala and G. ten Brinke, "Functional Materials Based on Self-Assembly of Polymeric Supramolecules," *Science* **295**, 2407–2409 (2002).

[8] G. M. Whitesides and B. Grzybowski, "Self-Assembly at All Scales," *Science* **295**, 2418–2421 (2002).

[9] R. Seemann et al., "Wetting morphologies and their transitions in grooved substrates," *J. Phys.: Condens. Matter* **23**, 184108 (2011).

[10] T.-G. Cha, J. W. Yi, M.-W. Moon, K.-R. Lee, and H.-Y. Kim, "Nanoscale patterning of microtextured surfaces to control superhydrophobic robustness," *Langmuir* **26**, 8319–8326 (2010).

[11] R. Z. Tan, A. Agarwal, N. Balasubramanian, D. L. Kwong, Y. Jiang, E. Widjaja, and M. Garland, "3D arrays of SERS substrate for ultrasensitive molecular detection," *Sens. Actuators A* **139**, 36–41 (2007).

[12] R. Soref, "The Past, Present, and Future of Silicon Photonics," *J. Select. Topics Quantum Electron.* **12**, 1678–1687 (2006).

[13] H. A. Atwater and A. Polman, "Plasmonics for improved photovoltaic devices," *Nat. Mater.* **9**, 205–213 (2010).

[14] J. Czochralski, "A new method for the measurement of crystallization rate of metals," *Z. Phys. Chem.* **92**, 219–221 (1918).

[15] V. E. Krohn and G. R. Ringo, "Ion source of high brightness using liquid metal," *Appl. Phys. Lett.* **27**, 479–481 (1975).

[16] C. A. Volkert and A. M. Minor, "Focused Ion Beam Microscopy and Micromachining," *MRS Bull.* **32**, 389–399 (2007).

[17] A. A. Tseng, "Recent developments in micromilling using focused ion beam technology," *J. Micromech. Microeng.* **14**, R15–R34 (2004).

[18] J. Goldstein, D. E. Newbury, D. C. Joy, C. E. Lyman, P. Echlin, E. Lifshin, L. Sawyer, and J. R. Michael, *Scanning Eelctron Microscopy and X-Ray Analysis* (Springer, New York, 2003), 3rd edition.

[19] L. A. Giannuzzi and F. A. Stevens, *Introduction to Focused Ion Beams: Instrumentation, Theory, Techniques and Practice* (Springer Science, Boston, 2005).

[20] J. F. Ziegler and J. P. Biersack, *SRIM – The Stopping and Range of Ions in Matter* (2008), http://www.srim.org/.

[21] J. M. Pavkovich, "Proximity effect correction calculations by the integral equation approximate solution method," *J. Vac. Sci. Technol. B* **4**, 159–163 (1986).

[22] H. Kuwano, "Dry development of resists exposed to low-energy focused gallium ion beam," *J. Appl. Phys.* **55**, 1149–1154 (1984).

[23] S. Matsui, K. Mori, K. Saigo, T. Shiokawa, K. Toyoda, and S. Namba, "Lithographic approach for 100 nm fabrication by focused ion beam," *J. Vac. Sci. Technol. B* **4**, 845–849 (1986).

[24] N. Koshida, Y. Ichinose, K. Ohtaka, M. Komuro, and N. Atoda, "Microlithographic behavior of transition metal oxide resists exposed to focused ion beam," *J. Vac. Sci. Technol. B* **8**, 1093–1096 (1990).

[25] K. Arshak, M. Mihov, D. Sutton, A. Arshak, and S. B. Newcomb, "Negative resist image by dry etching: a novel surface imaging resist scheme," *Microelectron. Eng.* **67–68**, 130–139 (2003).

[26] Z. Liu, K. Iltanen, N. Chekurov, K. Grigoras, and I. Tittonen, "Aluminum oxide mask fabrication by focused ion beam implantation combined with wet etching," *Nanotechnology* **24**, 175304 (2013).

[27] E. D. Palik, J. W. Faust, Jr., H. F. Gray, and R. F. Greene, "Study of the Etch-Stop Mechanism in Silicon," *J. Electrochem. Soc.* **129**, 2051–2059 (1982).

[28] B. Schmidt, S. Oswald, and L. Bischoff, "Etch Rate Retardation of Ga+-Ion Beam-Irradiated Silicon," *J. Electrochem. Soc.* **152**, G875–G879 (2005).

[29] S. Takahashi, M. Ohashi, S. Fukatsu, Y. Shiraki, and R. Ito, "Sub-100 nm pattern formation using a novel lithography with SiN_x resist by focused ion beam exposure and dry-etching development," *J. Vac. Sci. Technol. B* **11**, 268–274 (1993).

[30] H.-Y. Lee and H.-B. Chung, "Ga+ focused-ion-beam exposure and CF_4 reactive-ion-etching development of Si_3N_4 resist optimized by Monte Carlo simulation," *J. Vac. Sci. Technol. B* **16**, 1161–1166 (1998).

[31] N. Chekurov, K. Grigoras, A. Peltonen, S. Franssila, and I. Tittonen, "The fabrication of silicon nanostructures by local gallium implantation and cryogenic deep reactive ion etching," *Nanotechnology* **20**, 065307 (2009).

[32] B. Wagner, H. J. Quenzer, W. Henke, W. Hoppe, and W. Pilz, "Microfabrication of complex surface topographies using grey-tone lithography," *Sens. Actuators A* **46–47**, 89–94 (1995).

[33] B. Morgan, C. M. Waits, J. Krizmanic, and R. Ghodssi, "Development of a Deep Silicon Phase Fresnel Lens Using Gray-Scale Lithography

and Deep Reactive Ion Etching," *J. Microelectromech. Syst.* **13**, 113–120 (2004).

[34] K. Totsu, K. Fujishiro, S. Tanaka, and M. Esashi, "Fabrication of three-dimensional microstructure using maskless gray-scale lithography," *Sens. Actuators A* **130–131**, 387–392 (2006).

[35] T. Zentgraf, Y. Liu, M. H. Mikkelsen, J. Valentine, and X. Zhang, "Plasmonic Luneburg and Eaton lenses," *Nat. Nanotechnol.* **6**, 151–155 (2011).

[36] A. J. van Roosmalen, J. A. G. Baggerman, and S. J. H. Brader, *Dry Etching for VLSI* (Plenum Press, New York, 1991).

[37] E. Forsén, Z. J. Davis, M. Dong, S. G. Nilsson, L. Montelius, and A. Boisen, "Dry release of suspended nanostructures," *Microelectron. Eng.* **73–74**, 487–490 (2004).

[38] T. Suntola and J. Hyvärinen, "Atomic Layer Epitaxy," *Ann. Rev. Mater. Sci.* **15**, 177–195 (1985).

[39] R. L. Puurunen, "Surface chemistry of atomic layer deposition: A case study for the trimethylaluminum/water process," *J. Appl. Phys.* **97**, 121301 (2005).

[40] S. M. George, "Atomic Layer Deposition: An Overview," *Chem. Rev.* **110**, 111–131 (2010).

[41] M. D. Groner, F. H. Fabreguette, J. W. Elam, and S. M. George, "Low-Temperature Al_2O_3 Atomic Layer Deposition," *Chem. Mater.* **16**, 639–645 (2004).

[42] K. Grigoras, L. Sainiemi, J. Tiilikainen, A. Säynätjoki, V-M. Airaksinen, and S. Franssila, "Application of ultra-thin aluminum oxide etch mask made by atomic layer deposition technique," *J. Phys.: Conf. Ser.* **61**, 369–373 (2007).

[43] M. K. Tripp, C. Stampfer, D. C. Miller, T. Helbling, C. F. Herrmann, C. Hierold, K. Gall, S. M. George, and V. M. Bright, "The mechanical properties of atomic layer deposited alumina for use in micro- and nano-electromechanical systems," *Sens. Actuators A* **130–131**, 419–429 (2006).

[44] L. Sainiemi, K. Grigoras, and S. Franssila, "Suspended nanostructured alumina membranes," *Nanotechnology* **20**, 075306 (2009).

[45] J. Aarik, A. Aidla, T. Uustare, and V. Sammelselg, "Morphology and structure of TiO_2 thin films grown by atomic layer deposition," *J. Cryst. Growth* **148**, 268–275 (1995).

[46] G. Triani, J. A. Campbell, P. J. Evans, J. Davis, B. A. Latella, and R. P. Burford, "Low temperature atomic layer deposition of titania thin films," *Thin Solid Films* **518**, 3182–3189 (2010).

[47] J. Dekker, K. Kolari, and R. L. Puurunen, "Inductively coupled plasma etching of amorphous Al_2O_3 and TiO_2 mask layers grown by atomic layer deposition," *J. Vac. Sci. Technol. B* **24**, 2350–2355 (2006).

[48] A. Szeghalmi, M. Helgert, R. Brunner, F. Heyroth, U. Gösele, and M. Knez, "Atomic layer deposition of Al_2O_3 and TiO_2 multilayers for applications as bandpass filters and antireflection coatings," *Appl. Opt.* **48**, 1727–1732 (2009).

[49] T. Alasaarela, D. Korn, L. Alloatti, A. Säynätjoki, A. Tervonen, R. Palmer, J. Leuthold, W. Freude, and S. Honkanen, "Reduced propagation loss in silicon strip and slot waveguides coated by atomic layer deposition," *Opt. Express* **19**, 11529–11538 (2011).

[50] P. Stenberg, M. Roussey, P. Ryczkowski, G. Genty, S. Honkanen, and M. Kuittinen, "A merged photonic crystal slot waveguide embedded in ALD-TiO_2," *Opt. Express* **21**, 24154–24162 (2013).

[51] L. Pavesi and D. J. Lockwood, *Silicon Photonics* (Springer-Verlag, Germany, 2004).

[52] B. E. A. Saleh and M. C. Teich, *Fundamentals of Photonics* (Wiley, New Jersey, 2007), 2nd edition.

[53] H. Kogelnik and T. Li, "Laser Beams and Resonators," *Appl. Opt.* **5**, 1550–1567 (1966).

[54] O. Svelto, *Principles of Lasers* (Springer Science+Business Media, New York, 1998), translated by D. C. Hanna.

[55] D. Collandon, "On the reflectivity of a ray of light inside a parabolic liquid stream," *Comptes Rendus* **15**, 800–802 (1842).

[56] Image by A. R. Albrecht, University of New Mexico (First prize in 2012 Image Photo Contest by *Optics & Photonics News*).

[57] E. Snitzer, "Cylindrical Dielectric Waveguide Modes," *J. Opt. Soc. Am.* **51**, 491–498 (1961).

[58] E.-G. Neumann *Single-Mode Fibers: Fundamentals* (Springer-Verlag, Berlin, 1988).

[59] G. P. Agrawal *Fiber-Optic Communications Systems* (Wiley, New York, 2002), 3rd edition.

[60] M. A. Foster, K. D. Moll, and A. L. Gaeta, "Optimal waveguide dimensions for nonlinear interactions," *Opt. Express* **12**, 2880–2887 (2004).

[61] H. K. Tsang, C. S. Wong, T. K. Liang, I. E. Day, S. W. Roberts, A. Harpin, J. Drake, and M. Asghari, "Optical dispersion, two-photon absorption and self-phase modulation in silicon waveguides at 1.5μm wavelength," *Appl. Phys. Lett.* **80**, 416–418 (2002).

[62] R. Claps, D. Dimitropoulos, V. Raghunathan, Y. Han, and B. Jalali, "Observation of stimulated Raman amplification in silicon waveguides," *Opt. Express* **11**, 1731–1739 (2003).

[63] I.-W. Hsieh, X. Chen, X. Liu, J. I. Dadap, N. C. Panoiu, C.-Y. Chou, F. Xia, W. M. Green, Y. A. Vlasov, and R. M. Osgood, "Supercontinuum generation in silicon photonic wires," *Opt. Express* **15**, 15242–15249 (2007).

[64] G. P. Agrawal *Nonlinear Fiber Optics* (Academic Press, San Diego, 2001), 3rd edition.

[65] A. C. Turner, C. Manolatou, B. S. Schmidt, M. Lipson, M. A. Foster, J. E. Sharping, and A. L. Gaeta, "Tailored anomalous group-velocity dispersion in silicon channel waveguides," *Opt. Express* **14**, 4357–4362 (2006).

[66] E. Dulkeith, F. Xia, L. Schares, W. M. Green, L. Sekaric, and Y. A. Vlasov, "Group index and group velocity dispersion in silicon-on-insulator photonic wires," *Opt. Express* **14**, 3853–3863 (2006).

[67] C. M. B. Cordeiro, W. J. Wadsworth, T. A. Birks, and P. St. J. Russell, "Engineering the dispersion of tapered fibers for supercontinuum generation with a 1064 nm pump laser," *Opt. Lett.* **30**, 1980–1982 (2005).

[68] Q. Xu, B. Schmidt, S. Pradhan, and M. Lipson, "Micrometre-scale silicon electro-optic modulator," *Nature* **435**, 325–327 (2005).

[69] M. Iqbal, M. A. Gleeson, B. Spaugh, F. Tybor, W. G. Gunn, M. Hochberg, T. Baehr-Jones, R. C. Bailey, and L. C. Gunn, "Label-free biosensor arrays based on silicon ring resonators and high-speed optical scanning instrumentation," *J. Select. Topics Quantum Electron.* **16**, 654–661 (2010).

[70] F. Morichetti, A. Canciamilla, C. Ferrari, A. Samarelli, M. Sorel, and A. Melloni, "Travelling-wave resonant four-wave mixing breaks the limits of cavity-enhanced all-optical wavelength conversion," *Nat. Commun.* **2**, 296 (2011).

[71] A. Yariv, "Universal relations for coupling of optical power between microresonators and dielectric waveguides," *Electron. Lett.* **36**, 321–322 (2000).

[72] T. Barwicz, M. R. Watts, M. A. Popović, P. T. Rakich, L. Socci, F. X. Kärtner, E. P. Ippen, and H. I. Smith, "Polarization-transparent microphotonic devices in the strong confinement limit," *Nat. Photon.* **2**, 57–60 (2007).

[73] T. Claes, D. Vermeulen, P. De Heyn, K. De Vos, G. Roelkens, D. Van Thourhout, and P. Bienstman, "Towards a silicon dual polarization ring resonator sensor for multiplexed and label-free structural analysis of molecular interactions," *XI Conf. Opt. Chem. Sens. and Biosens.* **P-93**, 159 (2012).

[74] M. R. Watts, T. Barwicz, M. A. Popović, P. T. Rakich, L. Socci, E. P. Ippen, H. I. Smith, and F. Kaertner, "Microring-resonator filter with doubled free-spectral-range by two-point coupling," *Proc. CLEO* **1**, 273–275 (2005).

[75] W. R. Headley, G. T. Reed, F. Gardes, A. Liu, and M. Paniccia, "Enhanced polarisation-independent optical ring resonators on silicon-on-insulator," *Proc. SPIE* **5730**, 195–202 (2005).

[76] C. H. Kwan and K. S. Chiang, "Study of polarization-dependent coupling in optical waveguide directional couplers by the effective-index method with built-in perturbation correction," *J. Lightwave Technol.* **20**, 1018–1026 (2002).

[77] D. X. Xu, P. Cheben, A. Delâge, S. Janz, B. Lamontagne, E. Post, and W. N. Ye, "Polarization-insensitive MMI-coupled ring resonators

in silicon-on-insulator using cladding stress engineering," *Proc. SPIE* **6477**, 64770D (2007).

[78] T. Tamir and S. T. Peng, "Analysis and Design of Grating Couplers," *Appl. Phys.* **14**, 235–254 (1977).

[79] I. Moerman, P. P. Van Daele, and P. M. Demeester, "A Review on Fabrication Technologies for the Monolithic Integration of Tapers with III-V Semiconductor Devices," *J. Select. Topics Quantum Electron.* **3**, 1308–1320 (1997).

[80] X. Chen and H. K. Tsang, "Polarization-independent grating couplers for silicon-on-insulator nanophotonic waveguides," *Opt. Lett.* **36**, 796–798 (2011).

[81] D. Taillaert, P. Bienstman, and R. Baets, "Compact efficient broadband grating coupler for silicon-on-insulator waveguides," *Opt. Lett.* **29**, 2749–2751 (2004).

[82] K. A. Bates, L. Li, R. L. Roncone, and J. J. Burke, "Gaussian beams from variable groove depth grating couplers in planar waveguides," *Appl. Opt.* **32**, 2112–2116 (1993).

[83] W. S. Zaoui, A. Kunze, W. Vogel, M. Berroth, J. Butschke, F. Letzkus, and J. Burghartz, "Bridging the gap between optical fibers and silicon photonic integrated circuits," *Opt. Express* **22**, 1277–1286 (2014).

[84] T. Aoyagi, Y. Aoyagi, and S. Namba, "High-efficiency blazed grating couplers," *Appl. Phys. Lett.* **29**, 303–304 (1976).

[85] P. Mottier and S. Valette, "Integrated Fresnel lens on thermally oxidized silicon substrate," *Appl. Opt.* **20**, 1630–1634 (1981).

[86] S. M. Shank, F. T. Chen, M. Skvarla, H. G. Craighead, P. Cook, R. Bussjager, F. Haas, and D. A. Honey, "Multiple-level phase gratings fabricated using focused ion-beam milling and electron-beam lithography," *J. Vac. Sci. Technol. B* **12**, 3643–3647 (1994).

[87] Y. Fu and B. K. A. Ngoi, "Virtual gray-scale mask for fabrication of micro-optical elements via focused ion beam direct writing," *Opt. Eng.* **44**, 128002 (2005).

[88] J. Genzer and R. R. Bhat, "Surface-Bound Soft Matter Gradients," *Langmuir* **24**, 2294–2317 (2008).

[89] S. Krämer, H. Xie, J. Gaff, J. R. Williamson, A. G. Tkachenko, N. Nouri, D. A. Feldheim, and D. L. Feldheim, "Preparation of Protein Gradients through the Controlled Deposition of Protein-Nanoparticle Conjugates onto Functionalized Surfaces," *J. Am. Chem. Soc.* **126**, 5388–5395 (2004).

[90] M. J. Lercel, G. F. Redinbo, F. D. Pardo, M. Rooks, R. C. Tiberio, P. Simpson, H. G. Craighead, C. W. Sheen, A. N. Parikh, and D. L. Allara, "Electron beam lithography with monolayers of alkylthiols and alkylsiloxanes," *J. Vac. Sci. Technol. B* **12**, 3663–3667 (1994).

[91] T. Zhu, X. Fu, T. Mu, J. Wang, and Z. Liu, "pH-Dependent Adsorption of Gold Nanoparticles on p-Aminothiophenol-Modified Gold Substrates," *Langmuir* **15**, 5197–5199 (1999).

[92] C. K. Harnett, K. M. Satyalakshmi, and H. G. Craighead, "Low-energy electron-beam patterning of amine-functionalized self-assembled monolayers," *Appl. Phys. Lett.* **76**, 2466–2468 (2000).

[93] T. S. Tighe, J. M. Worlock, and M. L. Roukes, "Direct thermal conductance measurements on suspended monocrystalline nanostructures," *Appl. Phys. Lett.* **70**, 2687–2689 (1997).

[94] W. Fon, K. C. Schwab, J. M. Worlock, and M. L. Roukes, "Phonon scattering mechanisms in suspended nanostructures from 4 to 40 K," *Phys. Rev. B* **66**, 045302 (2002).

[95] L. Shi, D. Li, C. Yu, W. Jang, D. Kim, Z. Yao, P. Kim, and A. Majumdar, "Measuring Thermal and Thermoelectric Properties of One-Dimensional Nanostructures Using a Microfabricated Device," *J. Heat Transfer* **125**, 881–888 (2003).

[96] B. Guha, C. Otey, C. B. Poitras, S. Fan, and M. Lipson, "Near-Field Radiative Cooling of Nanostructures," *Nano Lett.* **12**, 4546–4550 (2012).

[97] Q. Chen, Y. D. Yang, and Y. Z. Huang, "Distributed mode coupling in microring channel drop filters," *Appl. Phys. Lett.* **89**, 061118 (2006).

[98] A. Delâge, D. X. Xu, R. W. McKinnon, E. Post, P. Waldron, J. Lapointe, C. Storey, A. Densmore, S. Janz, B. Lamontagne, P. Cheben, and J. H. Schmid, "Wavelength-dependent model of a ring resonator sensor excited by a directional coupler," *J. Lightwave Technol.* **27**, 1172–1180 (2009).

[99] COMSOL, Inc., Burlington, MA., USA, *COMSOL Multiphysics*. http://www.comsol.com/.

[100] M. Bass *Handbook of Optics, vol. 2*. (McGraw-Hill Professional, USA, 1995), 2nd edition.

[101] M. A. Foster, A. C. Turner, M. Lipson, and A. L. Gaeta, "Nonlinear optics in photonic nanowires," *Opt. Express* **16**, 1300–1320 (2008).

[102] S. M. Stavis, E. A. Strychalski, and M. Gaitan, "Nanofluidic structures with complex three-dimensional surfaces," *Nanotechnology* **20**, 165302 (2009).

[103] V. Jokinen and S. Franssila, "Capillarity in microfluidic channels with hydrophilic and hydrophobic walls," *Microfluid Nanofluid* **5**, 443–448 (2008).

[104] A. Shevchenko, V. Ovchinnikov, and A. Shevchenko, "Large-area nanostructured substrates for surface enhanced Raman spectroscopy," *Appl. Phys. Lett.* **100**, 171913 (2012).

[105] C. L. C. Smith, B. Desiatov, I. Goykmann, I. Fernandez-Cuesta, U. Levy, and A. Kristensen, "Plasmonic V-groove waveguides with Bragg grating filters via nanoimprint lithography," *Opt. Express* **20**, 5696–5706 (2012).

[106] K. H. Rasmussen, S. S. Keller, F. Jensen, A. M. Jorgensen, and O. Hansen, "SU-8 etching in inductively coupled oxygen plasma," *Microelectron. Eng.* **112**, 35–40 (2013).

[107] K. Keskinbora, C. Grévent, U. Eigenthaler, M. Weigand, and G. Schütz, "Rapid Prototyping of Fresnel Zone Plates via Direct Ga+ Ion Beam Lithography for High-Resolution X-ray Imaging," *ACS Nano* **7**, 9788–9797 (2013).

[108] L. H. Gabrielli and M. Lipson, "Integrated Luneburg lens via ultra-strong index gradient on silicon," *Opt. Express* **19**, 20122–20127 (2011).

[109] B. Bai, X. Meng, J. Laukkanen, T. Sfez, L. Yu, W. Nakagawa, H. P. Herzig, L. Li, and J. Turunen, "Asymmetrical excitation of surface plasmon polaritons on blazed gratings at normal incidence," *Phys. Rev. B* **80**, 035407 (2009).

[110] Q. Gan, Y. Gao, K. Wagner, D. Vezenov, Y. J. Ding, and F. J. Bartoli, "Experimental verification of the rainbow trapping effect in adiabatic plasmonic gratings," *Proc. Natl. Acad. Sci. U.S.A.* **108**, 5169–5173 (2011).

[111] N. C. Lindquist, T. W. Johnson, D. J. Norris, and S.-H. Oh, "Monolithic Integration of Continuously Tunable Plasmonic Nanostructures," *Nano Lett.* **11**, 3526–3530 (2011).

[112] G. Lagubeau, M. Le Merrer, C. Clanet, and D. Quáré, "Leidenfrost on a ratchet," *Nat. Phys.* **7**, 395–398 (2011).

[113] J. T. Ok, E. Lopez-Oña, D. E. Nikitopoulos, H. Wong, and S. Park, "Propulsion of droplets on micro- and sub-micron ratchet surfaces in the Leidenfrost temperature regime," *Microfluid. Nanofluid.* **10**, 1045–1054 (2011).

[114] A. H. J. Yang, S. D. Moore, B. S. Schmidt, M. Klug, M. Lipson, and D. Erickson, "Optical manipulation of nanoparticles and biomolecules in sub-wavelength slot waveguides," *Nature* **457**, 71–75 (2009).

[115] F. Xia, M. Rooks, L. Sekaric, and Y. Vlasov, "Ultra-compact high order ring resonator filters using submicron silicon photonic wires for on chip optical interconnects," *Opt. Express* **15**, 11934–11941 (2007).

[116] M. Peccianti, A. Pasquazi, Y. Park, B. E. Little, S. T. Chu, D. J. Moss, and R. Morandotti, "Demonstration of a stable ultrafast laser based on a nonlinear microcavity," *Nat. Commun.* **3**, 765 (2012).

[117] J. Safioui, F. Leo, B. Kuyken, S-P. Gorza, S. K. Selvaraja, R. Baets, P. Emplit, G. Roelkens, and S. Massar, "Supercontinuum generation in hydrogenated amorphous silicon waveguides at telecommunication wavelengths," *Opt. Express* **22**, 3089–3097 (2014).

[118] L. Karvonen, A. Säynätjoki, Y. Chen, H. Jussila, J. Rönn, M. Ruoho, T. Alasaarela, S. Kujala, R. A. Norwood, N. Peyghambarian, K. Kieu, and S. Honkanen, "Enhancement of the third-order optical nonlinearity in ZnO/Al_2O_3 nanolaminates fabricated by atomic layer deposition," *Appl. Phys. Lett.* **103**, 031903 (2013).

BUSINESS +
ECONOMY

ART +
DESIGN +
ARCHITECTURE

SCIENCE +
TECHNOLOGY

CROSSOVER

DOCTORAL
DISSERTATIONS